The Astrophysical Journal, 984:35 (18pp), 2025 May 1 https://doi.org/10.3847/1538-4357/adc37a

Limb-brightened Jet in M87 from Anisotropic Nonthermal Electrons

Yuh Tsunetoe[1,2], Dominic W. Pesce[1,3], Ramesh Narayan[1,3], Andrew Chael[4], Zachary Gelles[5], Charles Gammie[6], Eliot Quataert[7], and Daniel Palumbo[1,3]
[1] Black Hole Initiative at Harvard University, 20 Garden Street, Cambridge, MA 02138, USA; ytsunetoe@fas.harvard.edu
[2] Center for Computational Sciences, University of Tsukuba, 1-1-1 Tennodai, Tsukuba, Ibaraki 305-8577, Japan
[3] Center for Astrophysics | Harvard & Smithsonian, 60 Garden Street, Cambridge, MA 02138, USA
[4] Princeton Gravity Initiative, Jadwin Hall, Princeton University, Princeton, NJ, USA
[5] Department of Physics, Princeton University, Princeton, NJ 08540, USA
[6] Astronomy Department and Physics Department, University of Illinois, 1110 West Green Street, Urbana, IL 61801, USA
[7] Department of Astrophysical Sciences, Princeton University, Princeton, NJ, USA

Received 2025 January 24; revised 2025 March 8; accepted 2025 March 19; published 2025 April 23

Abstract

Very long baseline interferometry observations reveal that relativistic jets like the one in M87 have a limb-brightened, double-edged structure. Analytic and numerical models struggle to reproduce this limb-brightening. We propose a model in which we invoke anisotropy in the distribution function of synchrotron-emitting nonthermal electrons such that electron velocities are preferentially directed parallel to magnetic field lines, as suggested by recent particle-in-cell simulations of electron acceleration and the effects of synchrotron cooling. We assume that the energy injected into nonthermal electrons is proportional to the jet Poynting flux, and we account for synchrotron cooling via a broken power-law energy distribution. We implement our emission model in both general relativistic magnetohydrodynamic (GRMHD) simulations and axisymmetric force-free electrodynamic (GRFFE) jet models and produce simulated jet images at multiple scales and frequencies using polarized general relativistic radiative transfer. We find that the synchrotron emission is concentrated parallel to the local helical magnetic field and that this feature produces limb-brightened jet images on scales ranging from tens of microarcseconds to hundreds of milliarcseconds in M87. We present theoretical predictions for horizon-scale M87 jet images at 230 and 345 GHz that can be tested with next-generation instruments. Due to the scale-invariance of the GRMHD and GRFFE models, our emission prescription can be applied to other targets and serve as a foundation for a unified description of limb-brightened synchrotron images of extragalactic jets.

Unified Astronomy Thesaurus concepts: Black hole physics (159); Plasma jets (1263); Radiative transfer (1335); Particle astrophysics (96); Active galactic nuclei (16)

1. Introduction

The active galactic nucleus (AGN) Messier 87* (hereafter M87*) in the giant elliptical galaxy Messier 87 is a prime target for the study of relativistic jets from black holes (BHs). As a relatively nearby AGN ($D = 16.9$ Mpc) with an extremely massive central BH ($M_\bullet = 6.2 \times 10^9 M_\odot$; Event Horizon Telescope Collaboration et al. 2019a, 2021a), M87* offers the opportunity of directly imaging and studying a relativistic jet from extragalactic scales down to the launching region just outside the event horizon. In M87*, the projected gravitational radius is $\theta_g = r_g/D \approx 3.8\ \mu$as,[8] which is larger than for any other known BH except the Galactic center BH Sagittarius A* ($\theta_g \approx 5\ \mu$as). M87* has a powerful jet ($P_{\rm jet} \approx 10^{43}$erg s^{-1}) that is observed in all bands of the electromagnetic spectrum (e.g., H. L. Marshall et al. 2002; D. E. Harris & H. Krawczynski 2006; E. S. Perlman et al. 2011; A. Abramowski et al. 2012). It is thus an excellent target for investigating the physics of relativistic jets, and in particular, for attempting to validate the Blandford-Znajek process (R. D. Blandford & R. L. Znajek 1977) as the central acceleration mechanism in BH jets.

In this context, the successful direct imaging of the central BH in M87* by the Event Horizon Telescope (EHT; Event Horizon Telescope Collaboration et al. 2019a, 2019b, 2019c,2019d, 2019e, 2019f, 2021a, 2021b, 2023) is a landmark achievement that has opened a window to the physics of jet acceleration, formation, and emission on scales just outside the central supermassive black hole. Upcoming observations with projects like the next-generation EHT (ngEHT; S. S. Doeleman et al. 2023) and the black hole Explorer (BHEX; M. D. Johnson et al. 2024) are expected to monitor the dynamics of the innermost regions of the jet, where the relativistic magnetized outflow emerges from the BH ergosphere.

High-resolution observations at multiple frequencies, covering a wide range of length scales from subparsec to kiloparsecs, have revealed that the M87 jet persistently shows limb-brightening. This is seen from the jet-launching region on submilliarcsecond (mas) scales (K. Hada et al. 2016; J. Y. Kim et al. 2018; R. C. Walker et al. 2018; R.-S. Lu et al. 2023) all the way up to galactic scales of hundreds of mas (A. S. Nikonov et al. 2023; see also the triple-edge jet in K. Hada 2017). In transverse profiles of the intensity, the jet has a large limb-to-spine[9] intensity ratio of ∼2–5 on submas scales (J.-S. Kim et al. 2024a) and ∼2–3 on the scale of several mas (R. C. Walker

---

[8] Throughout, we use the gravitational length scale $r_g \equiv GM_\bullet/c^2$ and timescale $t_g \equiv GM_\bullet/c^3$, where $M_\bullet$ is the black hole mass.

[9] We refer to the central region of the jet near its axis as the spine, and the region near the transverse jet boundary as the limb or the edge.

et al. 2018). Most VLBI observations of other jet sources do not resolve structure across the jet width. However, in those jets that are resolved in the transverse direction, prominent limb-brightening has been detected (e.g., 3C 84; G. Giovannini et al. 2018, Centaurus A; M. Janssen et al. 2021, NGC 315; J. Park et al. 2024). These observational results suggest that limb-brightening may be a universal feature of BH jets.

Meanwhile, there has been a persistent discrepancy between the observations and theoretical models. Theoretical studies using general relativistic magnetohydrodynamic (GRMHD) simulations and radiative transfer (GRRT) calculations indicate that a nonthermal component is required in the electron energy distribution function (eDF) to obtain detectable emission over an extended region of the jet, as observed in M87* at millimeter wavelengths (J. Davelaar et al. 2019; A. Cruz-Osorio et al. 2022). However, these studies find, and we also confirm in previous work, that standard prescriptions for the nonthermal electron eDF do not reproduce the strongly accented limb-brightened jet images seen in M87. Rather, they produce single-edged or even spine-brightened jets (Y. Tsunetoe et al. 2025; see also C. M. Fromm et al. 2022; M. Zhang et al. 2024 for surveys of nonthermal electron prescriptions). Recently, H. Yang et al. (2024) examined the inner jet morphology with nonthermal electrons accelerated by the electric current density and cooled by synchrotron radiation. They obtained limb-brightening of the jet at around 1 mas from the core when they considered a very rapidly spinning BH with $a_* \equiv a/M = 0.98$. However, models with moderate spin ($a_* = 0.5$) and zero spin did not show limb-brightening.

Limb-brightened jets on large scales have also been studied with force-free electrodynamic (FFE) models (e.g., A. Tchekhovskoy et al. 2008; A. E. Broderick & A. Loeb 2009). K. Takahashi et al. (2018) obtained a symmetrical double-edged jet for a BH with an extremely high spin ($a_* = 0.998$), assuming nonthermal electron injection at a location far ($80r_g$) from the jet axis and the BH, to avoid asymmetric emission due to the rotational motion of jet plasma. As yet, there is no unified model of BH jets that can produce limb-brightened images for a range of BH spin values and over a range of scales from near the BH horizon to galactic scales.

In this paper, we consider a new approach to modeling the emission from jets. We assume that the nonthermal electrons in the jet have a highly *anisotropic* distribution, with velocities parallel to the magnetic field vastly exceeding perpendicular velocities. Particle-in-cell (PIC) simulations of relativistic magnetically dominated plasma turbulence show that electrons are accelerated into a nonthermal, power-law eDF with a strong anisotropy in their pitch angle with respect to the local magnetic field (L. Comisso & L. Sironi 2021, 2022). A. Galishnikova et al. (2023) implemented anisotropic thermal synchrotron emission and absorption in GRRT image calculations and explored its effect on the image. They surveyed three kinds of kinetic-scale instability inducing the anisotropy in the accretion disk, and pointed out that the precise choice can affect the size of the BH ring image.

In this work, we implement anisotropy in the eDF of nonthermal electrons in the jet and study the effect of this anisotropy on the jet image. We model synchrotron emission and absorption from anisotropic power-law-distributed electrons and carry out GRRT ray-tracing to calculate theoretical M87 jet images over a range of scales using both GRMHD simulations and general relativistic FFE (GRFFE) models. We show that anisotropic nonthermal electrons naturally produce limb-brightened jets in a variety of scenarios.

We introduce the GRMHD and GRFFE models in Sections 2.1 and 2.2, our model of nonthermal electrons in Section 2.3, and the GRRT calculations in Section 2.4. We demonstrate in Section 3.1 that anisotropy in the eDF of nonthermal electrons is essential for producing limb-brightening in the jet image with GRMHD models. Then, in Section 3.2, we compare the model images with existing observations and present theoretical predictions for what we might see with more sensitive and better resolved future observations. We also confirm in Section 3.3, using the GRFFE model, that jet limb-brightening persists in the model up to galactic scales, as seen in observations. Finally, Section 4 is dedicated to a discussion of applications of the model and future prospects, along with concluding remarks.

2. Method

We work with two kinds of models: GRMHD models and GRFFE models. GRMHD models (described in Section 2.1) take the density, temperature, velocity, and magnetic field strength from a GRMHD simulation, and supplement these with a prescription (Section 2.3) for nonthermal electrons in the jet. GRFFE models (Section 2.2) use an analytical general relativistic force-free electrodynamics model of a time-stationary, axisymmetric jet (A. Tchekhovskoy et al. 2008; Z. Gelles et al. 2025), and use the same prescription (Section 2.3) for nonthermal electrons.

The GRMHD models enable us to study individual snapshots as well as time variations. They are our preferred choice for modeling observations and studying jet dynamics close to the BH. GRMHD snapshots can also be summed to obtain time-averaged results. However, these models are reliable only out to $r \sim 10^3 r_g$, or projected angular offsets ∼1 mas in M87. The GRFFE models, on the other hand, can be extended to arbitrarily large distance from the BH (we go out to $\sim 10^5 r_g$ in this paper). However, since they assume a steady state, they are limited to time-averaged studies. Apart from these differences, a feature of the present work is that we use the same prescriptions to model the heating and cooling of nonthermal electrons in both the GRMHD and GRFFE models. Thus, in principle, for the same object, we can use the GRMHD model close to the BH and switch to the GRFFE model at larger distances.

2.1. GRMHD Model

We use the same data sets as in Y. Tsunetoe et al. (2025), viz., the magnetically arrested disk (MAD; I. V. Igumenshchev et al. 2003; R. Narayan et al. 2003; A. Tchekhovskoy et al. 2011; F. Yuan & R. Narayan 2014) GRMHD simulations reported in R. Narayan et al. (2022). We focus on two representative BH spin values: $a_* = +0.9$ and $+0.5$. We set the BH mass $M = 6.2 \times 10^9 M_\odot$ (Event Horizon Telescope Collaboration et al. 2019a, 2021a) and the mass-accretion rate $\dot{M} = 5 \times 10^{-4} M_\odot\ \mathrm{yr}^{-1}$ for $a_* = +0.9$ and $\dot{M} = 1.1 \times 10^{-3} M_\odot\ \mathrm{yr}^{-1}$ for $a_* = +0.5$ (we discuss below how we estimate $\dot{M}$), as appropriate for M87*. For each simulation, we consider a subset of 100 snapshots that cover a duration of $5000\, t_g$, which corresponds to about five years in M87*.

In each GRMHD snapshot, we divide the simulation volume into a region with low magnetization $\sigma \equiv B^2/4\pi\rho c^2 \leqslant 1$, and a region with high $\sigma > 1$. We identify the former with the disk and the sub-relativistic wind and assume that the electrons there are purely thermal. We use the "R-β" prescription from M. Mościbrodzka et al. (2016),

$$R \equiv \frac{T_{\rm i}}{T_{\rm e}} = R_{\rm low}\frac{1}{1+\beta^2} + R_{\rm high}\frac{\beta^2}{1+\beta^2}, \tag{1}$$

to determine the electron temperature $T_{\rm e}$, assuming the adiabatic indices of electrons and ions to be $4/3$ and $5/3$, respectively. Here, $T_{\rm i}$ is the ion temperature and β is the thermal-to-magnetic pressure ratio. We set $R_{\rm low} = 10$ and $R_{\rm high} = 160$ based on the model scoring results shown in Table 3 in Event Horizon Telescope Collaboration et al. (2021a), which indicate that both $a_* = 0.9$ and 0.5 models with these parameters "pass" the polarimetric and other constraints used in that study.

We identify the $\sigma > 1$ region of a snapshot with the relativistic jet. GRMHD simulations have numerical difficulties in this region because of the low gas density, which requires the application of an artificial density floor. Despite this complication, the simulations are believed to provide accurate results for quantities like the fluid velocity, magnetic field strength, and Poynting flux. We therefore use the velocity and magnetic field data from the GRMHD simulation, but ignore the less-reliable density and temperature data. As an added motivation for neglecting the simulated thermal electrons, we note that the radiation from jets is known to be dominated by nonthermal emission, and nonthermal electrons are not modeled as a separate population in most GRMHD simulations (but see A. A. Chael et al. 2017). We estimate the electron number density and Lorentz factor distribution of the nonthermal electrons from the local Poynting flux, as described in Section 2.3 and Appendix A.

Apart from limiting the nonthermal electrons to the region with $\sigma > 1$, we also apply an upper cutoff σ_m so that the radiating region lies between $1 < \sigma < \sigma_m$. The motivation is to limit the radiating zone to a sheath near the outer edge of the jet, based on the expectation that most of the dissipation and particle acceleration is likely to take place at this boundary. We choose

$$\sigma_{\rm m} = \frac{300}{\sqrt{r}}. \tag{2}$$

This gives a large cutoff σ_m near the BH, covering the region where nonthermal electrons are preferentially injected by the Poynting flux (Section 2.3). At large radii, σ_m becomes small (e.g., ~10 at $r = 10^3\,r_{\rm g}$).

Since GRMHD simulations are scale-free, we follow the usual practice of adjusting $\dot{M}$ so as to satisfy a luminosity constraint obtained from observations. In the present work, we set the mass-accretion rate onto the BH in the $a_* = 0.9$ model to $\dot{M} = 5 \times 10^{-4} M_\odot\ {\rm yr}^{-1}$, which gives an average flux density of ~0.5 Jy at 230 GHz for purely thermal electrons restricted to $\sigma \leqslant 1$. This flux density matches EHT measurements of M87*. For the $a_* = 0.5$ model, we correspondingly set $\dot{M} = 1.1 \times 10^{-3} M_\odot\ {\rm yr}^{-1}$. Both of these $\dot{M}$ values are in good agreement with the corresponding estimates ($8 \times 10^{-4} M_\odot\ {\rm yr}^{-1}$, $1.6 \times 10^{-3} M_\odot\ {\rm yr}^{-1}$, respectively) given in Table 3 in Event Horizon Telescope Collaboration et al. (2021a). The small differences are consistent with the natural variability we expect in simulations, given that the Event Horizon Telescope Collaboration et al. (2021a) work was based on an earlier set of GRMHD simulations run with the `iharm` code (C. F. Gammie et al. 2003; S. C. Noble et al. 2006), whereas our work is based on the simulations from R. Narayan et al. (2022), which used different initial conditions and were run with the `KORAL` code (A. Sadowski et al. 2013, 2014).

In Section 3, we show images corresponding to the $a_* = +0.9$ GRMHD simulation, and treat this as our fiducial model. We discuss the second model with $a_* = +0.5$ in Section 4.

2.2. GRFFE Model

To describe the properties of the jet on scales larger than those accessible to GRMHD simulations, we employ an axisymmetric GRFFE model in which the fluid inertia and internal energy are negligible and only electromagnetic forces are dynamically relevant. We use the GRFFE jet model developed by Z. Gelles et al. (2025), which builds on earlier work by A. Tchekhovskoy et al. (2008) and A. E. Broderick & A. Loeb (2009) and extends the model to a Kerr spacetime. This model provides a description of the jet geometry, magnetic field structure, and bulk fluid Lorentz factor throughout the jet.

The magnetic field structure in the GRFFE model is determined by the so-called "magnetic stream function" ψ, which is related to the azimuthal component of the vector potential by $\psi = A_\phi$.[10] For an axisymmetric system, ψ must satisfy a second-order differential equation (see I. Okamoto 1974; R. Narayan et al. 2007) that admits the approximate solution,

$$\psi(r,\theta) \propto \begin{cases} r^{2-2s}\,[1-\cos(\theta)], & 0 \leqslant \theta \leqslant \frac{\pi}{2} \\ r^{2-2s}\,[1+\cos(\theta)], & \frac{\pi}{2} < \theta \leqslant \pi \end{cases}, \tag{3}$$

which is accurate to $\lesssim$10% for both nonrotating and rotating systems in the flat space limit (A. Tchekhovskoy et al. 2008). The specification of 2–$2s$ for the radial power-law index ensures that at large r the magnetic field lines follow a jet shape described by

$$R \propto z^s, \tag{4}$$

such that $s = 0.5$ corresponds to a parabolic jet and $s = 1$ corresponds to a conical jet. For this paper, we adopt a value of $s = 0.6$, which is consistent with VLBI measurements of the M87 jet (e.g., K. Hada et al. 2013, 2016; M. Nakamura et al. 2018). The magnetic field is determined from ψ following Equation (6) in Z. Gelles et al. (2025). All magnetic field lines in the GRFFE model live on contours of constant ψ, and the field lines that intersect the black hole horizon at poloidal angle $\theta = \pi/2$ define the edge of the jet.

To set the overall normalization of the magnetic field, we assume that the total jet power—measured from the integrated Poynting flux in both jets—is equal to

$$P_J = 1.4 a_*^2 \dot{M} c^2, \tag{5}$$

---

[10] This expression for ψ is appropriate for the Boyer–Lindquist coordinates used in the Z. Gelles et al. (2025) GR model, though we note that some previous papers (e.g., R. Narayan et al. 2007; A. Tchekhovskoy et al. 2008) used orthonormal coordinates in flat space such that, in those coordinates, $\psi = R A_\phi$.

where $\dot{M}$ is the mass-accretion rate onto the black hole. The coefficient 1.4 is appropriate for accretion in the magnetically arrested disk (MAD) state (A. Tchekhovskoy et al. 2011; R. Narayan et al. 2022). We use the same value of $\dot{M}$ as in the GRMHD model. Also, we assume that the jet radiation is produced by nonthermal electrons, which we model using the local Poynting flux, as in the GRMHD model. Details are given in Section 2.3.

The magnetic field lines rotate rigidly (V. C. A. Ferraro 1937) at a rate determined by the black hole's spin and the location at which the field lines thread the horizon (e.g., R. D. Blandford & R. L. Znajek 1977). The fluid motion perpendicular to magnetic field lines is set by the force-free condition to be the so-called "drift velocity," which can be analytically determined from the known E- and B-fields (e.g., J. C. McKinney 2006; R. Narayan et al. 2007; A. Chael et al. 2023). However, the force-free condition does not by itself constrain the component of the fluid motion parallel to the magnetic field lines, which has thus often been assumed to be zero (e.g., A. Tchekhovskoy et al. 2008; A. E. Broderick & A. Loeb 2009). For our GRFFE model, we instead use the prescription from Z. Gelles et al. (2025) that assigns a value for the parallel fluid motion using an energy conservation argument in the force-free limit of cold GRMHD; see Z. Gelles et al. (2025) for details.

Unlike in GRMHD, the Lorentz factor of plasma bulk motion $\gamma_{\rm bulk}$ in the GRFFE model can grow very large ($\gamma_{\rm bulk} \gg 1$) far away from the BH, reaching ~20–80 at $z \sim 10^4$–$10^5 r_g$. To allow for drag on the jet at its boundaries, we suppress $\gamma_{\rm bulk}\beta_{\rm bulk}$ by a factor of 0.5[11] throughout the entire GRFFE jet, where $\beta_{\rm bulk}$ is the bulk velocity. In addition, we set a hard ceiling of $\gamma_{\rm bulk} \leqslant 6$.[12] Together, the velocity suppression and ceiling produce fluid Lorentz factors in the GRFFE model that are closer to those found in the GRMHD simulations. Furthermore, we confirm in Section 3.3 that the suppression and ceiling are favored in comparison with observed images of the M87 jet, which serves as a validation of the prescription here.

In analogy with the sigma cutoff σ_m applied in the GRMHD model, we exclude the spine region in the GRFFE model as well. We cut out the region with

$$\psi(r, \theta) < \psi(r_{\rm fp}, \theta_{\rm fp}) \tag{6}$$

for the northern jet, and the symmetrical region in the southern hemisphere; here, $r_{\rm fp} = r_{\rm H}$, the horizon radius, and $\theta_{\rm fp}$ is set to 65°. This corresponds to a cutoff of the inner ~80% of the jet width at large distances.

2.3. Nonthermal Electrons in the Jet

The GRMHD and GRFFE models describe the structure of the magnetic field and fluid velocity throughout the jet, but they need to be supplemented with a model for the number density and energy distribution of synchrotron-emitting electrons. There is strong observational evidence that the radiation we observe from jets is produced primarily by nonthermal (power-law) electrons and that these electrons are continuously accelerated throughout the length of the jet, probably through dissipative interactions with the surrounding medium (e.g., A. H. Bridle & R. A. Perley 1984). With this in mind, we assume the following prescriptions for the heating and subsequent synchrotron cooling of nonthermal electrons (Appendix A discusses additional details).

In the interest of simplicity, we make a number of approximations. We assume that the energy to heat the electrons in the jet comes from the jet power, for which we use the Poynting flux $\boldsymbol{S}$ in the Zero-Angular-Momentum Observer (ZAMO) frame as a proxy (see Appendix C for details). This quantity is readily available in both the GRMHD and GRFFE models. The dissipation of jet power is likely related to "frictional" drag exerted on the relativistic jet by instabilities where it meets the external medium (which is either a slowly moving wind, or a stationary ambient medium); the actual mechanism of particle acceleration may be related to magnetic reconnection in the shear flow that will naturally develop at the jet boundary (e.g., L. Sironi et al. 2021). In this picture, we expect the bulk of the heating to occur in a relatively narrow region near the outer boundary of the jet. In the force-free region of a jet, the Poynting flux itself is largest at the outer edge and thus naturally introduces preferential edge-heating if we simply make the heating rate proportional to the Poynting flux. In addition, as explained in Sections 2.1 and 2.2, we accentuate the edge-heating effect by arbitrarily cutting out the central ("spine") region of the jet and setting the heating in this interior region to zero.

We adopt here the ansatz that some small fraction $h \ll 1$ of the jet power is converted per logarithmic interval of r into nonthermal electron energy density. In this spirit, we write the accumulated nonthermal electron energy density injected into a given jet fluid element as

$$u_{\rm nt,inj} = h\,\frac{|\vec{S}|}{c}. \tag{7}$$

To motivate this formula, the electromagnetic energy density associated with the Poynting flux is $|\boldsymbol{S}|/c$, and a fraction h of this energy density is injected in the form of nonthermal electrons.

We assume that the injected electrons have a power-law distribution of Lorentz factor γ of the form

$$f_{\rm inj}(\gamma) = \begin{cases} 0, & \gamma < \gamma_m \\ \frac{n_{\rm pl}(p-1)}{\gamma_m^{1-p} - \gamma_{\rm max}^{1-p}}\gamma^{-p}, & \gamma_m \leqslant \gamma \leqslant \gamma_{\rm max}. \\ 0, & \gamma > \gamma_{\rm max} \end{cases} \tag{8}$$

Here, γ_m and $\gamma_{\rm max}$ are the minimum and maximum Lorentz factors of the injected electrons. Equating the total energy in these electrons (including the rest mass energy, though the latter is small since the γ values we consider are large) to $u_{\rm nt,inj}$, we determine the power-law electron number density $n_{\rm pl}$ to be

$$n_{\rm pl} = \frac{u_{\rm nt,inj}(p-2)(\gamma_m^{1-p} - \gamma_{\rm max}^{1-p})}{m_e c^2 (p-1)(\gamma_m^{2-p} - \gamma_{\rm max}^{2-p})}. \tag{9}$$

The actual $f(\gamma)$ at any location in the jet is different from $f_{\rm inj}(\gamma)$ because of synchrotron cooling. The oldest injected electrons have cooled for a time on the order of the the characteristic

---

[11] The factor of 0.5 is a rough estimate, which we obtained by comparing the velocity profile in the GRMHD simulation with the corresponding velocity in the GRFFE model.

[12] Note that this hard ceiling differs from the prescription used in Z. Gelles et al. (2025), who instead apply a softer cutoff (see their Equation (49)).

dynamical time (assuming the jet travels at a speed $\sim c$),

$$t_c = \frac{r}{c}, \tag{10}$$

which corresponds to a synchrotron cooling Lorentz factor (see Equations (A3) and (A5) in Appendix A, as well as the associated caveat in a footnote):

$$\gamma_c \equiv \Gamma(t_c) = \frac{6\pi m_e c}{\sigma_T B^2 t_c}. \tag{11}$$

Electrons with injected Lorentz factors $\gamma > \gamma_c$ are able to cool to γ_c over a time t_c. For those electrons injected more recently and hence with ages $t < t_c$, the corresponding $\Gamma(t)$ is larger. The net $n(\gamma)$ is obtained by integrating over all ages between 0 and t_c. This is a standard problem in synchrotron theory (e.g., R. Sari et al. 1998) and results in a double power-law distribution of electron Lorentz factors.

Following R. Sari et al. (1998), we distinguish between two cooling regimes: a "slow-cooling" regime that corresponds to $\gamma_c \geqslant \gamma_m$, and a "fast-cooling" regime that corresponds to $\gamma_c < \gamma_m$. The corresponding electron energy distributions, $n_{\rm slow}(\gamma)$ and $n_{\rm fast}(\gamma)$, are given by Equations (A13) and (A14) in Appendix A.

The above model for the nonthermal electron energy distribution has four free parameters—h, p, γ_m, and $\gamma_{\rm max}$—where we may safely set $\gamma_{\rm max} \to \infty$ in most situations.[13] We use the same parameter values for both the GRMHD and GRFFE models, simply replacing the Poynting flux estimate appropriately for each model. We recognize that the present model is fairly unsophisticated, ignoring time dilation and other relativistic effects, but we feel that it is adequate for an initial trial model such as the present study.[14] The current model also assumes that the synchrotron cooling takes place in a constant-strength magnetic field, rather than one whose magnitude decreases with distance from the black hole (see Appendix A).

For this paper, we adopt $p = 2.5$ (a fairly standard value) for the power-law index and $\gamma_m = 30$, $\gamma_{\rm max} = 10^8$ for the minimum and maximum Lorentz factors of the injected electron distribution.[15] We set $h = 0.0025$ for the fiducial model ($a_* = 0.9$), which gives for the GRMHD model an average total flux density (thermal and nonthermal radiation) at 86 GHz of $\sim$1.1 Jy, in agreement with observations. In the secondary model ($a_* = 0.5$), we similarly find $h = 0.005$.

2.4. GRRT with Anisotropic Nonthermal Electrons

As mentioned in Section 1, a key feature of the present work is the inclusion of an anisotropic angular energy distribution for the nonthermal electrons in the jet. Here, we derive the synchrotron emission and absorption coefficients for an anisotropic power-law distribution of Lorentz factor γ, in an analogous way to the thermal case considered in A. Galishnikova et al. (2023). We consider here a single power-law energy distribution function and then apply the same analysis to the double power-law case in Appendix B.

Following A. Galishnikova et al. (2023), we write the anisotropic single power-law distribution function as

$$\begin{aligned} f(\gamma, \xi) &= N_{\rm pl}\left\{\sqrt{1 + \left(\frac{p_\perp}{m_e c}\right)^2 + \eta\left(\frac{p_\parallel}{m_e c}\right)^2}\right\}^{-p} \\ &= N_{\rm pl}\{\sqrt{1 + (\gamma^2 - 1)(\sin^2\xi + \eta \quad \cos^2\xi)}\}^{-p} \\ &\quad \times (\gamma_m < \gamma < \gamma_{\rm max}, \quad 0 \leqslant \xi \leqslant \pi). \end{aligned} \tag{12}$$

Here, γ and ξ are the Lorentz factor of an electron and the pitch angle of the electron's motion with respect to the magnetic field; $p_\perp = m_{\rm e} c\sqrt{\gamma^2 - 1}\,\sin\xi$ and $p_\parallel = m_{\rm e} c\sqrt{\gamma^2 - 1}\,\cos\xi$ are the relativistic momentum components perpendicular and parallel to the magnetic field; $N_{\rm pl}$ is a normalization factor with units of [cm^{-3}]; p is the power-law index; and γ_m and $\gamma_{\rm max}$ are the minimum and maximum Lorentz factors. The parameter η describes the degree and sense of anisotropy; $\eta < 1$ (or > 1) indicates that the motion of electrons is concentrated along (perpendicular to) the direction of the local magnetic field; $\eta = 1$ corresponds to the usual isotropic power-law distribution.

For large γ,

$$f(\gamma, \xi) = N_{\rm pl} \quad \gamma^{-p}\{1 + (\eta - 1)\cos^2\xi\}^{-p/2}. \tag{13}$$

Normalization by the total number density of power-law electrons $n_{\rm pl}$ gives

$$N_{\rm pl} = \frac{(p - 1)n_{\rm pl}}{\gamma_m^{1-p} - \gamma_{\rm max}^{1-p}} P(p, \eta)^{-1}, \tag{14}$$

$$P(p, \eta) = \frac{1}{2}\int_0^\pi {\rm d}\xi \quad \sin\xi\{1 + (\eta - 1)\cos^2\xi\}^{-p/2} \tag{15}$$

$$= \int_0^1 {\rm d}\mu \quad \{1 + (\eta - 1)\mu^2\}^{-p/2}. \tag{16}$$

Thus, the anisotropic single power-law distribution function can be written as

$$f(\gamma, \xi) = \phi(\xi) \quad f_{\rm iso}(\gamma), \tag{17}$$

where

$$\phi(\xi) = P(p, \eta)^{-1}\{1 + (\eta - 1)\cos^2\xi\}^{-p/2}, \tag{18}$$

and $f_{\rm iso}(\gamma)$ corresponds to the isotropic single power-law distribution function, i.e., Equation (13) with $\eta = 1$. Equation (17) takes a simpler form than the thermal case discussed in A. Galishnikova et al. (2023), in that it separates into the product of ξ- and γ-dependent parts, as assumed in D. B. Melrose (1971).

The anisotropic power-law emissivity is obtained by integrating the single particle emissivity with the distribution function in Equation (17). For the emitting electrons with large Lorentz factor, the synchrotron radiation is strongly beamed in the direction of the pitch angle $\xi \simeq \theta_B$, where θ_B is the angle between the light ray and the magnetic field. D. B. Melrose (1971) wrote down the emissivity and absorption coefficients expanded to the first order of γ^{-1} around $\xi = \theta_B$. In our case

---

[13] We cannot set $\gamma_{\rm max} \to \infty$ if $p \leqslant 2$, since the energy content in the injected electrons would diverge. For such values of p, $\gamma_{\rm max}$ should be treated as an important adjustable parameter. However, since in the present work we choose $p = 2.5$, we may set $\gamma_{\rm max}$ to any large value we please; we arbitrarily choose $\gamma_{\rm max} = 10^8$.

[14] All special and general relativistic effects are treated correctly when we do ray-tracing to calculate images. The only exception is that the ray-tracing code works in the "fast-light" approximation (see Section 2.4).

[15] The choice $\gamma_m = 30$ is informed by the following argument: The hot two-temperature accretion flow from which M87's jet originates has an electron temperature $T_e \sim$ few $\times$ 10^{10} K, for which the thermal Maxwell–Jüttner distribution function peaks at a Lorentz factor $\gamma_{\rm peak} \sim 10$. Assuming that the power-law distribution of the accelerated electrons in the jet begins a factor of a few above $\gamma_{\rm peak}$, we choose $\gamma_m = 30$.

with Equation (17), the full-Stokes synchrotron emissivities and absorption coefficients are obtained as[16]

$$j_I = \phi(\theta_B) \quad j_{I,\mathrm{iso}}, \tag{19}$$

$$j_Q = \phi(\theta_B) \quad j_{Q,\mathrm{iso}}, \tag{20}$$

$$j_U = 0, \tag{21}$$

$$j_V = \quad \phi(\theta_B) \quad \left\{1 + \frac{g(\theta_B)}{p+2}\right\} \quad j_{V,\mathrm{iso}}, \tag{22}$$

and

$$\alpha_I = \phi(\theta_B) \quad \alpha_{I,\mathrm{iso}}, \tag{23}$$

$$\alpha_Q = \phi(\theta_B) \quad \alpha_{Q,\mathrm{iso}}, \tag{24}$$

$$\alpha_U = \quad 0, \tag{25}$$

$$\alpha_V = \quad \phi(\theta_B) \quad \left\{1 + \frac{g(\theta_B)}{p+2}\right\} \quad \alpha_{V,\mathrm{iso}}\ , \tag{26}$$

where

$$g(\theta_B) = \tan\theta_B \frac{1}{\phi(\theta_B)} \frac{d\phi}{d\xi}\bigg|_{\xi=\theta_B} \tag{27}$$

$$= \frac{p(\eta - 1)\sin^2\theta_B}{1 + (\eta - 1)\cos^2\theta_B}\ . \tag{28}$$

Here, $j_{\{I,Q,V\},\mathrm{iso}}$ and $\alpha_{\{I,Q,V\},\mathrm{iso}}$ are the emissivities and absorption coefficients for the isotropic power-law case with minimum and maximum Lorentz factors γ_m and $\gamma_{\max}$ (see, for example, J. Dexter 2016, Appendix A2 in that paper). In Appendix B, we apply the above analysis to a broken, double power-law distribution of electrons.

We have implemented the full-polarization, anisotropic double power-law synchrotron emissivity and absorption coefficients in the GRRT code `SHAKO` (see Appendix of Y. Tsunetoe et al. 2024 for validation of the code), to calculate multiscale jet images based on the GRMHD and GRFFE models. We numerically tabulate the integrals in $j_{\{I,Q,V\},\mathrm{iso}}$ and $\alpha_{\{I,Q,V\},\mathrm{iso}}$, as in Y. Tsunetoe et al. (2024, 2025). For the Faraday rotation and conversion coefficients, we adopt the isotropic single power-law forms.

In this work, we assume that the nonthermal electrons are injected with $p = 2.5$, $\gamma_m = 30$, and $\gamma_{\max} = 10^8$, and that they have a highly anisotropic distribution with $\eta = 0.01$, while the thermal electrons are isotropic. A distribution with $\eta = 0.01$ corresponds to an average pitch angle of $\langle \sin^2 \xi \rangle \sim 0.2$ for $p = 2.5$, $\langle \sin^2 \xi \rangle \sim 0.1$ for $p = 3.5$ (relevant above the cooling break; see Equation (A13)), and $\langle \sin^2 \xi \rangle \sim 0.3$ for $p = 2$ (below the break in the fast-cooling regime; see Equation (A14)). We set the observer's inclination angle with respect to the BH spin axis to $i = 163°$ (R. C. Walker et al. 2018).

We note that our GRRT calculations are done under the usual "fast-light" approximation, in which one ignores propagation time differences between rays emerging from different cells in the GRMHD simulation volume. The fast-light approximation is equivalent to taking the speed of light to infinity. The more proper "slow-light" approach, which uses the correct finite light speed, is computationally more involved since the image observed at a given instant receives contributions from radiation emitted at different times, and hence from different snapshot outputs of the GRMHD simulation. For EHT applications, slow-light calculations are considered to be unnecessary since tests indicate that, at least for certain observables, slow-light introduces only small changes in the results relative to fast-light calculations (J. Dexter et al. 2010; T. Bronzwaer et al. 2018). However, for the study of beamed relativistic jets, as in the present work, the differences will be large and it is essential to include slow light in future work.

2.5. Expected Anisotropy in the Nonthermal Electron Population

In strongly magnetized, low-collisionality plasmas such as those found in jets, there are strong theoretical and empirical reasons to expect the plasma distribution function to be anisotropic with respect to the magnetic field. Empirically, such anisotropy is well-established in the solar corona and solar wind (S. D. Bale et al. 2009). The most extreme anisotropy is inferred via spectroscopy of coronal holes, which implies that oxygen ions have perpendicular temperatures ~10–100 times larger than their parallel temperatures (S. R. Cranmer et al. 1999). Note that this is the opposite sense of anisotropy as that invoked in the present paper, but there is no reason to expect oxygen heating in the solar corona and relativistic electron acceleration (and synchrotron cooling) in jets to produce the same anisotropy. The key point of this example is that very large anisotropies are observed in the strongly magnetized solar corona. As we now describe, several processes can generically generate anisotropy in the electron distribution function in jets. By contrast, there are few (if any) mechanisms known to robustly isotropize the plasma distribution function, precisely because the plasma is highly magnetized and low-collisionality.

Absent heating and cooling, adiabatic evolution of the distribution function will drive plasma anisotropy in a low-collisionality plasma. The adiabatic invariants for charged particle motion parallel ($j_\parallel$) and perpendicular ($j_\perp$) to the field are conserved for slow variations of the background state (e.g., P. A. Sturrock 1994). Following the appendix in M. Chandra et al. (2015), $j_\perp = p_\perp^2/\tilde{B}$ and $j^\parallel = (\tilde{B}/\tilde{\rho})p_\parallel$. Here, $p_\perp$, $p_\parallel$ are the momenta perpendicular and parallel to the field, and $\tilde{B}$ and $\tilde{\rho}$ are the ratio of magnetic field strength and density to their values in some reference state. As density and magnetic field strength evolve, conservation of $j_\parallel$, $j_\perp$ drives anisotropy.

For example, suppose $dn_e/d^3p \propto \gamma^{-p-2}$. Initially, in the ultra-relativistic limit, $\gamma^{-p-2} \sim (j_\perp + j_\parallel^2)^{-(p-2)/2}$. Since $j_\perp$, $j_\parallel$ are constant under slow evolution of the field strength and density, at later times $\gamma^2 \propto (p_\perp/\tilde{B} + p_\parallel^2(\tilde{B}/\tilde{\rho})^2)$. On comparing to Equation (12), we see that this implies the anisotropy parameter $\eta = \tilde{B}^3/\tilde{\rho}^2$.

The scaling factors $\tilde{B}$ and $\tilde{\rho}$ depend on jet shape and velocity. Suppose the jet is axisymmetric and has a purely toroidal magnetic field. If in cylindrical coordinates each streamline has $R \propto z^s$ and $v_z \propto z^a$, then one can show that $\tilde{\rho} = (z/z_0)^{-2s-a}$ and $\tilde{B} = (z/z_0)^{-s-a}$, so that $\eta = \tilde{B}^3/\tilde{\rho}^2 = (z/z_0)^{s-a}$. Then, for $s = 0.6$ in an unaccelerated ($a = 0$) jet, η *increases* downstream. If acceleration is constant ($a = 1$), however, η *decreases* downstream. Even then, anisotropy driving is weak: for an

---

[16] While the total and linear polarization emissivities and absorption coefficients given here are applicable in general, the expressions for circular polarization were obtained in the limit $\gamma_m \to 0$, $\gamma_{\max} \to \infty$, as in D. B. Melrose (1971), and are valid only in the frequency range $\nu_m \ll \nu \ll \nu_{\max}$. Although this approximate expression is sufficient for our present purposes, since this work focuses only on total intensity images, it is fairly straightforward to do a more accurate calculation for future applications by applying the correct limits in the double integral in $j_{V,\mathrm{iso}}$ and tabulating the results numerically.

initially isotropic distribution at $z_0 = r_g$, η is only 0.15 at $z = 100 r_g$. Although adiabatic driving of anisotropy is interesting because it links the electron anisotropy to the shape and velocity profile of the jet, it is likely too weak to produce the $\eta \sim 0.01$ assumed in our model.

Even if adiabatic evolution of the plasma can generate the needed anisotropy, another argument against it as the dominant source of anisotropy is that significant heating is needed to explain the surface brightness profiles of jets and the flat spectrum in the optically thick regime (e.g., R. D. Blandford & A. Königl 1979).

Synchrotron cooling will also generate anisotropy, as described in V. Zhdankin et al. (2023). The radiation reaction force preferentially reduces momentum perpendicular to the magnetic field, driving the plasma toward $\eta < 1$. For cooling to be effective, the cooling time must be shorter than the outflow time for electrons that produce synchrotron radiation at the frequencies of interest. In our GRMHD model for M87, the cooling time for electrons that produce 86 GHz emission and the dynamical time are equal at $r \sim 100 r_g$. At higher frequency and larger radius, cooling can be effective in driving anisotropy.

For a model in which particle injection by acceleration is balanced by cooling, the steady-state anisotropic distribution function for isotropic injection and (anisotropic) synchrotron cooling is $\propto (\sin^2\alpha)^{-1}\gamma^{-p-1}$, where p is the injection spectrum and we have assumed $p > 1$ (as is typically the case in most particle acceleration scenarios). This follows from the fact that the steady-state distribution function is proportional to the injection spectrum times the synchrotron cooling time: this steepens the spectrum by one power of γ and introduces the $1/\sin^2\alpha$ dependence. Note that this synchrotron-cooled steady-state distribution function is precisely of the form of Equation (17) with $\eta = 0$, except that strong synchrotron cooling fixes the $\sin^2\alpha$ dependence independent of the momentum power-law index.

A third source of electron anisotropy is the electron acceleration process itself. Particle-in-cell simulations of particle energization in strongly magnetized turbulent plasmas show that the electrons are preferentially accelerated along the local magnetic field, creating a pitch-angle anisotropy with $T_\parallel > T_\perp$ (L. Comisso & L. Sironi 2022). The same occurs in reconnection simulations with a significant mean magnetic field (L. Comisso & B. Jiang 2023). This effect is, however, less prominent at higher electron energies.

Pitch-angle scattering tends to restore isotropy in the distribution function. Both Coulomb scattering and wave–particle scattering in principle contribute. Isotropization will be effective when the scattering timescale is shorter than the anisotropy driving timescale. In jets, the densities are low and the electron energies are high, so Coulomb scattering can be safely neglected. Wave–particle scattering can in principle be produced by the ambient turbulent fluctuations. The properties of this scattering in relativistic plasma turbulence are not well-characterized. In the empirically well-studied case of the solar wind, however, wave–particle scattering appears to primarily be due to kinetic instabilities generated by large anisotropy in the distribution function (S. D. Bale et al. 2009), not fluctuations associated with the ambient turbulence. For example, the fluid firehose instability sets in if $P_\parallel - P_\perp \gtrsim B^2/4\pi$ (both non-relativistically and relativistically; e.g., A. Galishnikova et al. 2023). In our models, $\beta \sim 10^{-2}$, permitting large anisotropies in both ions and electrons. Driving by radiative cooling will, however, produce anisotropy in the electrons only, and particle acceleration may preferentially do so as well. The relevant instability is then a resonant electron-only version of the firehose instability. This has been studied in non-relativistic electron-ion plasmas (e.g., E. Camporeale & D. Burgess 2008) but not, to the best of our knowledge, in relativistic electron-ion or pair plasmas. Nonetheless, on energetic grounds—and by analogy to other such kinetic instabilities—we are confident that relatively large electron $T_\parallel/T_\perp$ will be kinetically stable in strongly magnetized jets.

3. Results

3.1. Time-averaged Images with the GRMHD Model

First, we demonstrate that anisotropy in nonthermal electrons is an essential ingredient in our GRMHD model for producing limb-brightened images in the jet-launching region in M87. The images shown below are based on our fiducial model with $a_* = 0.9$ (see Section 4 for the $a_* = 0.5$ model).

In Figure 1, we show time-averaged GRMHD images over a duration of $5000 t_g$ at 86 GHz made using purely thermal electrons in the disk and wind (which are defined as the region with magnetization $\sigma \leqslant 1$) and no radiation from the jet (top panel); thermal disk-wind and isotropic ($\eta = 1$) nonthermal electrons in the jet region (defined as $\sigma > 1$; second panel); thermal disk-wind and isotropic nonthermal electrons in the jet with a sigma cutoff following Equation (2) to enhance limb-brightening (third panel); and thermal disk-wind and anisotropic ($\eta = 0.01$) nonthermal electrons in the jet with the sigma cutoff of Equation (2) (bottom panel). As explained earlier, we set $M_\bullet = 6.2 \times 10^9 M_\odot$ and $\dot{M} = 5 \times 10^{-4} M_\odot\ \mathrm{yr}^{-1}$, and choose the observer's inclination angle to be $i = 163°$ (R. C. Walker et al. 2018).

We can clearly see in the top panel in Figure 1 that thermal synchrotron emission from the disk and wind produces a ring-like structure similar to that observed by the EHT at 230 GHz, but it does not produce much extended emission along the jet even though the $\sigma \leqslant 1$ wind extends out to a large distance.

Injection of nonthermal, power-law electrons in the jet ($\sigma > 1$) using the Poynting flux prescription of Section 2.3 with $h = 0.0025$, $p = 2.5$, $\gamma_m = 30$, $\gamma_{\max} = 10^8$ (second panel from the top in Figure 1) lights up a spatially extended jet feature in the image with broad and slightly asymmetric (bottom is brighter) emission out to ~1 mas. The asymmetry is triggered by helical bulk motion of the plasma in the jet, which gives rise to stronger relativistic Doppler beaming in the approaching (here, bottom) side than the receding (upper) side. However, there is no sign of two-sided limb-brightening in the jet image.

The third panel in Figure 1 shows the effect of restricting the emission from the jet to a narrow sheath around its outer edge by applying the sigma cutoff prescription in Equation (2). Although one might expect that removing emission from the spine region of the jet would contribute to a significantly more limb-brightened and symmetrical jet image, we continue to find a broad and asymmetric jet with no sign of limb-brightening. The broad ridge emission in the image comes from the foreground jet sheath, which produces strong isotropic synchrotron emission in a direction perpendicular to the helical magnetic field. The asymmetry remains due to a combination of relativistic Doppler beaming and the magnetic field

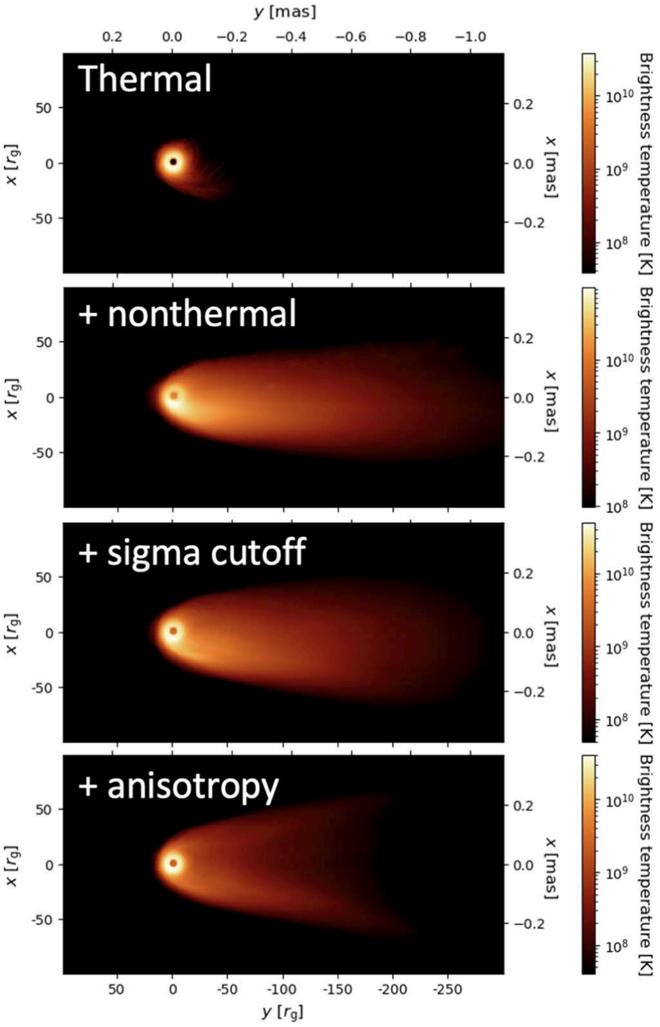

Figure 1. Time-averaged images of the M87* BH and its jet at 86 GHz, based on the $a_* = 0.9$ GRMHD model, for four electron energy distribution prescriptions. Top panel: assumes thermal electrons in the disk and wind, which are defined as the region with magnetization $\sigma \leqslant 1$, and no radiation from the jet, which is defined as the region with $\sigma > 1$. Second panel: thermal electrons in the disk and wind, and nonthermal electrons in the jet, modeled as described in Section 2.3. Third panel: thermal electrons in the disk and wind, and nonthermal electrons in the jet, but with the jet emission limited to a sheath by means of a sigma cutoff, $1 < \sigma < 300/\sqrt{r}$. Bottom panel: Same as the third panel, but introducing a strong anisotropy, with $\eta = 0.01$, in the energy distribution of the nonthermal electrons in the jet. This is the only model that produces a limb-brightened jet image similar to what is seen in time-averaged observations (see bottom right panel in Figure 4).

geometry; the helicity of the magnetic fields (caused by frame dragging from the spinning BH) makes the local field lines more aligned with the line of sight on the receding side of the jet, producing weaker emission than on the approaching side. Thus, we would not observe a symmetric jet image in the isotropic case, even without relativistic Doppler beaming.

Finally, as shown in the bottom panel in Figure 1, when we introduce anisotropy in the nonthermal electron distribution, we do obtain a limb-brightened jet image, similar to what is observed in M87 (compare with the bottom right panel in Figure 4). Here, synchrotron radiation from a population of nonthermal electrons with strong anisotropy ($\eta = 0.01$) produces emission that is concentrated in directions that are aligned with the local magnetic field lines. The result is a brightening of both jet edges, where the magnetic field is more closely aligned with the line of sight and a suppression of the emission from the foreground sheath region, where the field lines are perpendicular to the line of sight. In particular, the anisotropy now advantages the debeamed (upper) side of the jet, in which the magnetic fields are more aligned with the line of sight. Notably, this means that the two symmetrical edges of the jet are brightened by two different mechanisms: Doppler beaming on the approaching side, and anisotropic emission aligned with the magnetic field on the receding side.

All the model images shown in the rest of the paper assume anisotropic nonthermal electrons with $\eta = 0.01$, and all the GRMHD model images include the sigma cutoff in Equation (2).[17]

3.2. Snapshot Images with the GRMHD Model

In Figure 2, we show images at 86 and 43 GHz corresponding to a snapshot from the $a_* = 0.9$ GRMHD simulation, and compare them with observations of M87 from J.-S. Kim et al. (2024a, 2024b). The model images are convolved with circular Gaussian beams of 40 and 80 μas, respectively, to approximately match the angular resolution of the observed images.[18]

The model images show edge-brightening in the jet, though the contrast between the emission at the jet edge and that in the jet center is lower than in the observational images. We see a number of spiral-shaped components bridging the two edges of the jet; these components originate from the foreground and background sides of the jet sheath, and seemingly analogous features are also seen in the corresponding observational images, though they are more stretched out along the jet.

In this context, it should be noted that our GRRT calculations are based on the fast-light approximation (see Section 2.4), under which some of the features in the GRMHD snapshot images are expected to be distorted. Specifically, a slow-light calculation will tend to stretch out features longitudinally parallel to the projected jet axis. The amount of stretching will depend on how relativistic the jet motion is, but could be considerable and might well give a better qualitative match between the simulated and observed images. In future dynamical studies of the M87 jet using data from GRMHD simulations, it will be crucial to use the slow-light ray-tracing.

Another noteworthy feature in Figure 2 is that the counter-jet component is noticeably fainter in the model images compared to the observational images, a property that also holds for the GRFFE-based images on larger scales (see Section 3.3). We discuss this issue in Section 4 in the context of the BH spin-dependence and the prescription for emission anisotropy.

Figure 3 shows GRMHD snapshot images at the high observing frequencies and fine angular resolutions that are expected to be achievable with next-generation submillimeter VLBI observations with ngEHT (S. S. Doeleman et al. 2023)

---

[17] An image corresponding to a constant sigma cutoff, $\sigma_m = 25$ (a relatively large value suggested by the work of A. Chael 2024), is shown in Appendix D. It demonstrates that the sigma cutoff contributes very little to the observed limb-brightening in the image.

[18] Note that the observational images from J.-S. Kim et al. (2024a, 2024b) were reconstructed using the `RESOLVE` imaging algorithm (P. Arras et al. 2018), which, unlike the more traditional `CLEAN` algorithm does not explicitly convolve (or "restore") the images using a specified Gaussian beam. Instead, the angular resolution in the reconstructed images is determined by a combination of the data quality and the parameterized image correlation structure, and in general, the resolution may even be a function of location within the image.

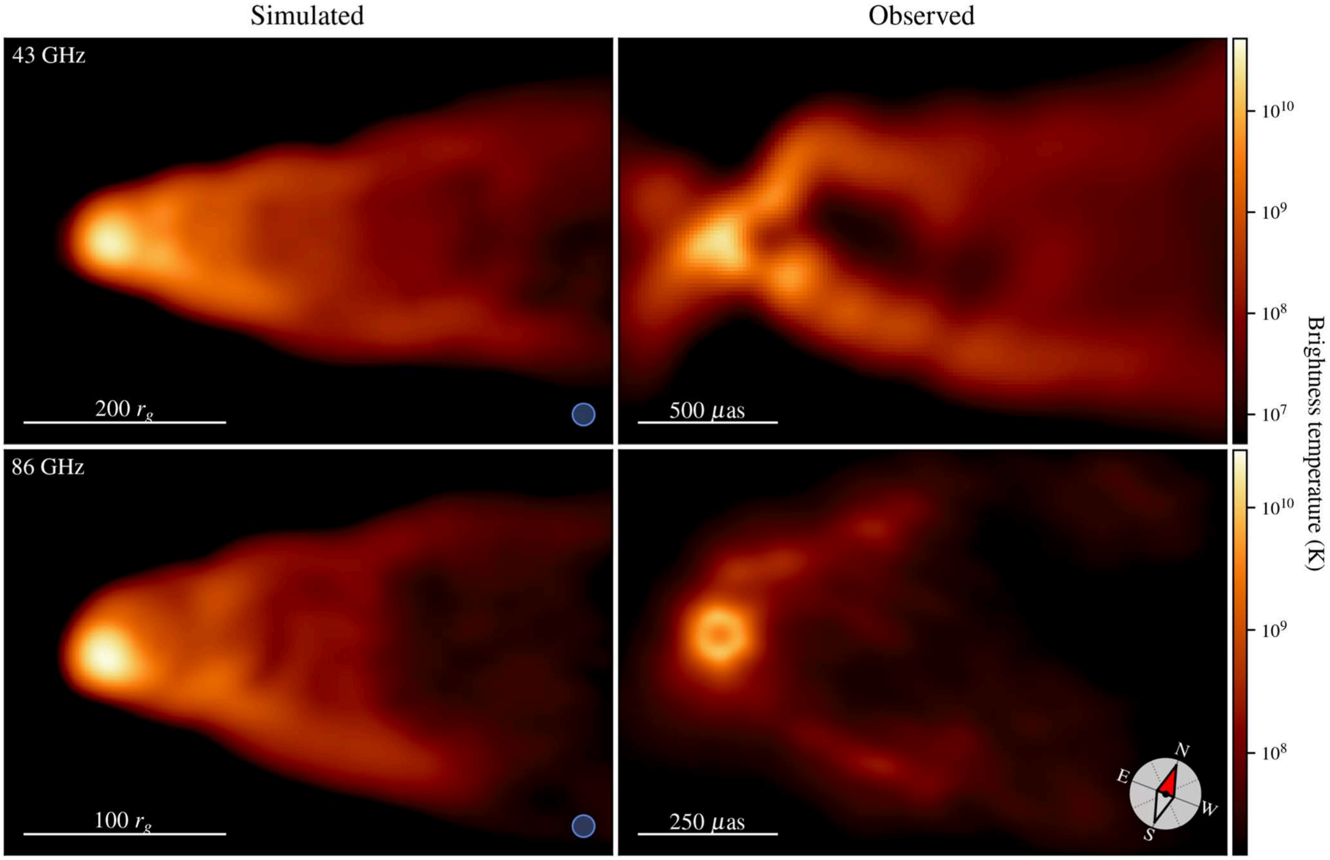

Figure 2. Comparison between images from a snapshot of the $a_* = 0.9$ GRMHD simulation (left column) and single-epoch observed images (right column) of the M87 jet structure at 43 GHz (top row) and 86 GHz (bottom row). The left and right images in each row share a common field of view, with the spatial scale indicated using a scale bar in units of r_g (for the simulated images) or μas (for the observed images). We blur the simulated images with circular Gaussian beams of FWHM 40 μas and 80 μas at 86 GHz and 43 GHz, respectively, to approximately match the resolution of the observed images; the FWHM contours for the convolving beams are shown in the lower right-hand corners of the simulated images. The 43 GHz observed image comes from VLBA observations conducted by R. C. Walker et al. (2018) and imaged by J.-S. Kim et al. (2024b), and the 86 GHz observed image comes from GMVA observations conducted by R.-S. Lu et al. (2023) and imaged by J.-S. Kim et al. (2024a). The images have been rotated by 21° so that the jet structure is approximately horizontal; cardinal directions are indicated by the compass on the lower right.

and the proposed space-based mission BHEX (M. D. Johnson et al. 2024). From top to bottom, Figure 3 shows model images at 86, 230, and 345 GHz blurred to angular resolutions on the left of 40, 20, and 15 μas, as appropriate for ngEHT, and angular resolutions on the right of 10, 6, and 4 μas, for BHEX. At these submillimeter wavelengths, plasma in the jet-launching region is optically thin, producing bright ring emission and fainter extended jet emission. As a result, we observe arm-like jet components originating from the foreground side of the jet sheath; these components are pronounced in the 230 and 345 GHz images. The arc-like features arise from particularly bright material loaded onto individual field lines, whose propagation traces the magnetic field structure along the jet. Movies made from a sequence of snapshots show the structures moving away from the BH. In this case, slow-light GRRT imaging will again be essential for quantitative comparisons with observations.

3.3. Images with the GRFFE Model

Our GRMHD simulations are only appropriate for spatial scales closer to the BH than $z \lesssim 10^3 r_g$, so we switch to the GRFFE fluid model for describing structure on larger scales. Figure 4 shows a comparison between the GRFFE model images and corresponding M87 observations at 8, 15, 43, and 86 GHz (J. Y. Kim et al. 2018; R. C. Walker et al. 2018; A. S. Nikonov et al. 2023). At a glance, the model images show qualitative agreement with the observations in the general shape, brightness, and limb-brightening, and also in the sense and degree of limb (a)symmetry in the approaching jet.

In the 86 and 43 GHz panels of Figure 4, the jet shows a weak asymmetry on several-mas scales in which the approaching (bottom) edge is modestly brighter than the receding (upper) edge. The symmetry apparent at the innermost radii results from a combination of resolution limitations and a balance between the two limb-brightening effects described in Section 3.1: Doppler beaming (enhancing emission along the lower edge of the jet) and field-aligned emission (enhancing emission along the upper edge of the jet). The asymmetry between the two jet limbs that is evident at larger radii in the 86 GHz image (and to a lesser extent in the 43 GHz image) arises because, at these intermediate radii, the magnetic field is not yet purely toroidal and the velocity field is not yet purely radial (as occurs farther downstream in the jet). In this particular GRFFE model, the Doppler beaming that enhances the lower edge of the jet turns out to be moderately more powerful than the anisotropic emission that enhances the upper edge of the jet. Our model does not produce counter-jet emission that is bright enough to match what is seen in the 43 GHz observed image.

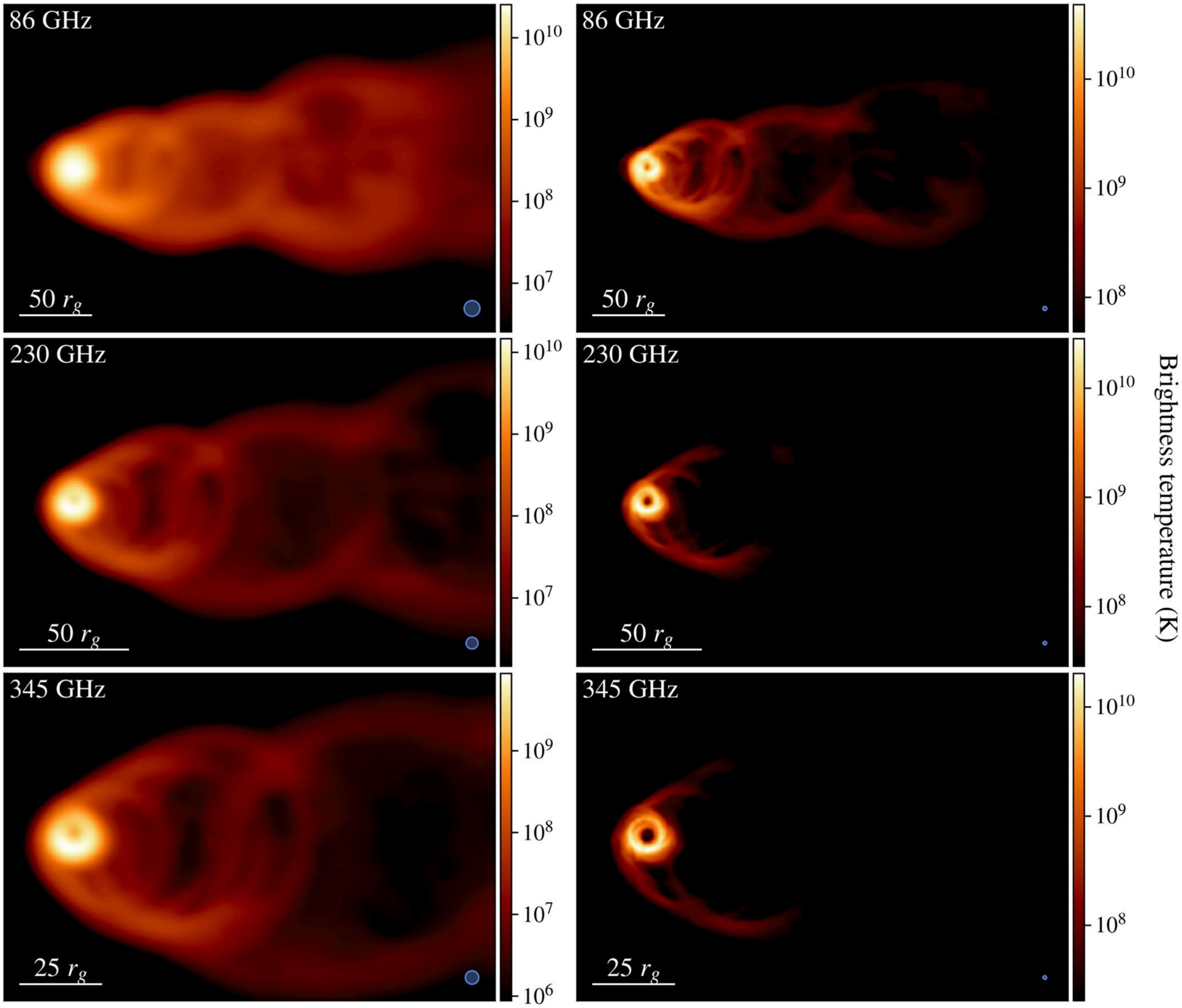

Figure 3. Left: Snapshot images from the $a_* = 0.9$ GRMHD simulation at 86, 230, and 345 GHz, blurred with circular Gaussian beams of 40, 20, and 15 μas, respectively, as appropriate for future ngEHT ground-based observations. Right: Same as the left, but blurred with smaller beams of 10, 6, and 4 μas, appropriate for the projected resolution of the future BHEX space VLBI mission. Note that the range of brightness temperatures is different in the left and right columns, and that we use a different snapshot here than the one shown in Figure 2.

At larger scales—as illustrated by the 15 and 8 GHz images in Figure 4—the model produces a symmetrical double-edged jet that extends out to hundreds of milliarcseconds. In regions of the jet far outside the light cylinder, the bulk plasma velocity is ultra-relativistic with predominantly poloidal motion, while the magnetic fields are almost purely toroidal (A. E. Broderick & A. Loeb 2009; K. Takahashi et al. 2018). This combination leads to strong, symmetrically beamed emission along both jet limbs and suppressed emission from the central ridge. We once again find that the counter-jet emission in the model is weaker than that in either the 8 or 15 GHz observations.

We confirmed that our fiducial model with a ceiling in the bulk velocity of $\gamma_{\rm bulk} = 6$ gives jet images that are consistent with the observations, whereas larger ceiling values cause the jet to appear truncated.[19] This can be understood as follows: the relativistic Doppler beaming factor for a purely longitudinal, approaching plasma bulk motion and an inclination angle i ($>90^\circ$) can be written as $g = 1/[\gamma_{\rm bulk}\{1 - \beta_{\rm bulk}\cos(180^\circ - i)\}]$, which for $i = 163^\circ$ peaks at $\gamma_{\rm bulk} \sim 3.5$ and decreases for larger $\gamma_{\rm bulk}$.[20] Thus, if the jet experiences unrestricted acceleration up to $\gamma_{\rm bulk} \gtrsim 10$ as predicted by the analytical GRFFE model, the observed intensity will decline rapidly in the outer jet and the model would be inconsistent with the extended jet images seen in M87. This is confirmed by observations of kinematics in the M87 jet that suggest bulk Lorentz factor values below 10 in the regions within $z \lesssim 10^5 r_g$ (J. Park et al. 2019).

4. Discussion and Conclusions

In this paper, we present a model capable of producing the limb-brightening seen in observations of astrophysical jets launched from black holes, and we demonstrate that our model

---

[19] By contrast, it was confirmed that the suppression factor does not require fine-tuning and is set to a straightforward value of 0.5.

[20] This also implies that we may preferentially observe jet components with $\gamma_{\rm bulk} \sim 3$–4 if there is a differential longitudinal velocity distribution in the outer M87 jet.

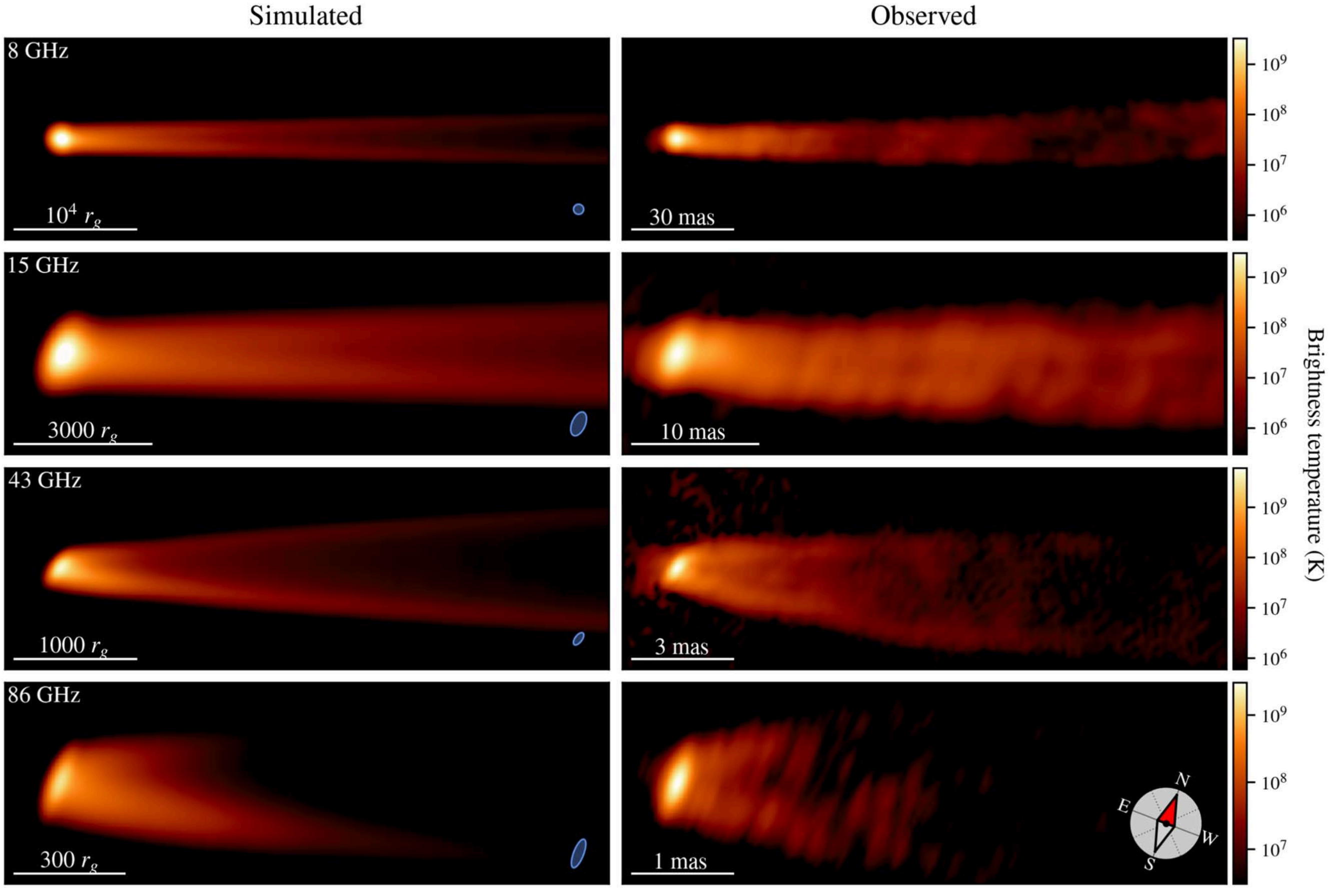

Figure 4. Comparison between simulated GRFFE images (left column) and observed images (right column) of the M87 jet across four frequencies and at matched spatial scales; from top to bottom, the observing frequencies are 8, 15, 43, and 86 GHz. We blur the simulated images using an elliptical Gaussian with the same parameters as the restoring beam used for the corresponding observed images; the FWHM contours for the convolving beams are shown in the lower right-hand corners of the simulated images. The 8 and 15 GHz observed images come from single-epoch VLBA observations imaged by A. S. Nikonov et al. (2023); the 43 GHz observed image comes from multi-epoch time-averaged VLBA observations imaged by R. C. Walker et al. (2018); and the 86 GHz observed image comes from multi-epoch time-averaged GMVA observations imaged by J. Y. Kim et al. (2018), including also HSA observations from K. Hada et al. (2016). All images have been rotated by 21° so that the jet structure is approximately horizontal; cardinal directions are indicated by the compass on the lower right.

can qualitatively and quantitatively reproduce VLBI observations of the jet in the M87 system across more than an order of magnitude in observing frequency ($\sim$8–86 GHz) and at least 3 orders of magnitude in spatial scale ($\sim$0.2–200 mas). The radio emission from the jet in our model is synchrotron radiation from a population of nonthermal electrons, which derive their energy from the Poynting power in the jet and subsequently cool (via synchrotron radiation) to produce a number density that follows a double power-law distribution.

The key new ingredient in our model for producing jet limb-brightening is the inclusion of anisotropy in the electron energy distribution function, such that electrons with velocities parallel to magnetic field lines are strongly favored relative to electrons with perpendicular velocities. We model the magnetic field and bulk velocity of the plasma throughout the jet using both GRMHD (to describe small-scale and time-resolved structure) and GRFFE (to describe large-scale and time-averaged structure), and we compute the emission using GRRT with synchrotron emission and absorption coefficients appropriately modified to incorporate the anisotropy. As we demonstrate in Figure 1, anisotropy has a large effect on the degree of limb-brightening in the jet, and indeed is essential, within the framework of our model, to produce any limb-brightening at all.

The primary results of this paper are illustrated in Figures 2–4 and can be summarized as follows:

1. Our GRMHD model enables us to study jet structure and dynamics on spatial scales up to $z \approx 10^3\, r_g$. Figure 2 shows that individual snapshots from our GRMHD model can demonstrate qualitative similarity with corresponding observations of the M87 jet system, including the general shape of the jet and the presence of limb-brightening.
2. Figure 3 provides predictions for the appearance of the M87 jet as seen with next-generation ground- and space-based high-frequency VLBI observations.
3. Our GRFFE model is applicable only to time-averaged jet structure but can describe arbitrarily large spatial scales. Figure 4 shows that images from our GRFFE model can reproduce the shape and brightness of the M87 jet out to scales of nearly $\sim 10^5 r_g \approx 250$ mas. The presence of limb-brightening and the magnitude of its asymmetry are also qualitatively consistent with observations.

Of the two different values of the BH spin that we explore in this paper, we find that our "fiducial" $a_* = 0.9$ model produces images that appear somewhat more consistent with the available M87 observations than those from our $a_* = 0.5$ model, so Figures 2–4 present images from the fiducial

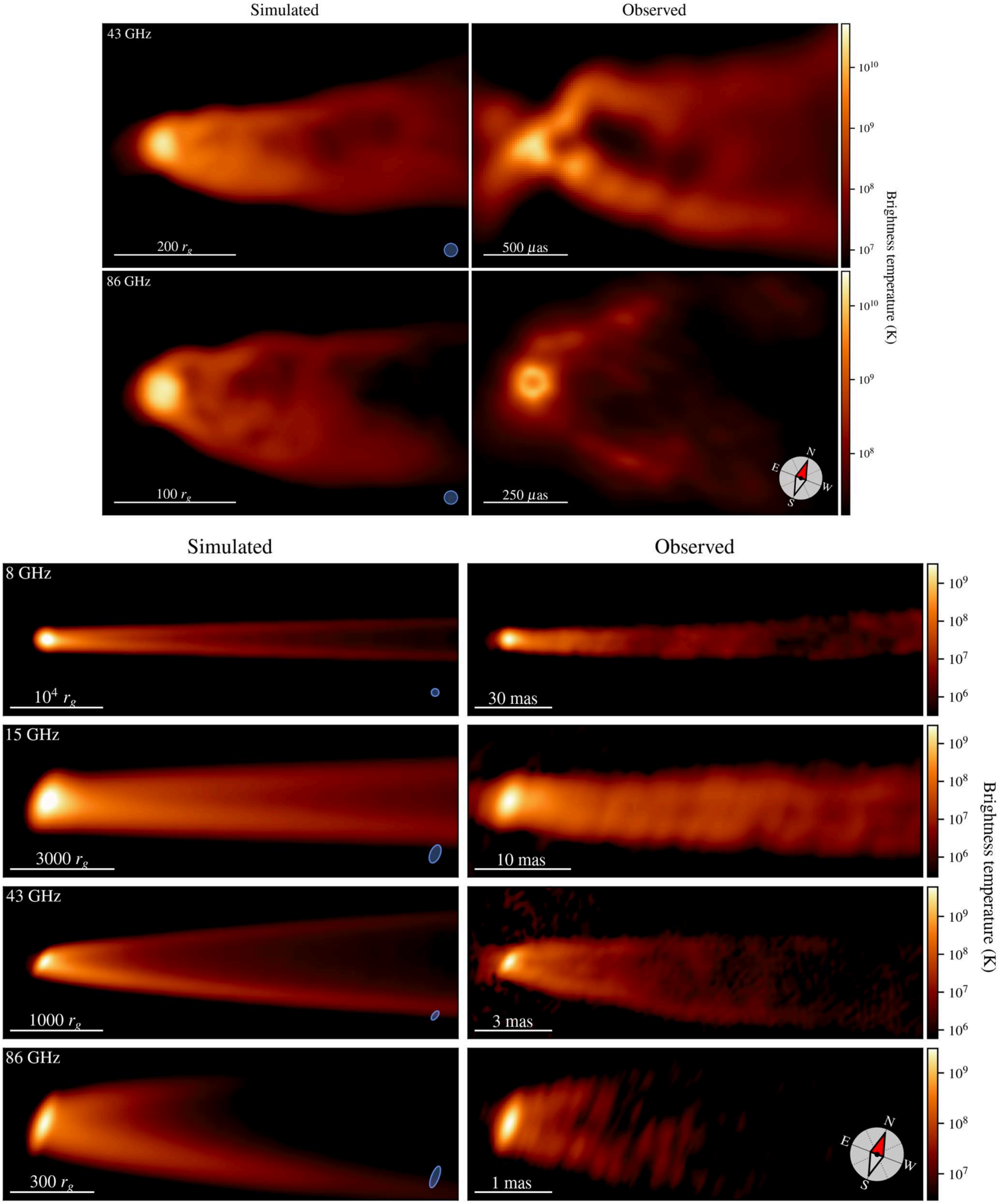

Figure 5. Same as Figure 2 (top) and Figure 4 (bottom), but for the moderate spin ($a_* = 0.5$) model.

$a_* = 0.9$ model. A comparison between our model images and the observations for the $a_* = 0.5$ case is shown in Figure 5.

In this paper, we have focused primarily on the ability of anisotropic synchrotron emission to yield limb-brightened jet structures, showing that GRMHD and GRFFE jet models coupled to strongly ($\eta = 0.01$) anisotropic GRRT can produce images that look like observations of M87 across a range of frequencies and spatial scales. However, we have not comprehensively explored the space of potential model variants, instead adopting simple treatments where possible for a number of the model parameters.

For instance, we use only a single value of the anisotropy parameter η for all nonthermal electrons in our model, rather than coupling the value of η to, e.g., plasma-β or other physical parameters (as in A. Galishnikova et al. 2023). We have not explored the effect of varying the minimum Lorentz factor γ_m of the injected nonthermal electrons (see Section 2.3). Our treatment of the bulk plasma velocity in the GRFFE model is also simplistic, with a simple ad hoc scaling factor applied to suppress the velocities to near-GRMHD levels (see Section 2.2). Perhaps because of these limitations, the present version of our model exhibits some points of disagreement with observations; in particular, our model struggles to produce images with a counter-jet as prominent as the one seen in observations.[21] We leave it to future work to explore whether increased model sophistication or physical self-consistency can alleviate such disagreements.

Limitations notwithstanding, we have shown here that a conceptually simple modification to otherwise fairly standard GRMHD or GRFFE jet models can generically produce the limb-brightening phenomenon that has been so ubiquitous in observations of jetted systems and yet so difficult to reproduce in simulations. And by virtue of the scale-invariance of GRMHD and GRFFE, our model is applicable to jetted BH systems beyond just M87 through appropriate choice of the underlying model parameters (BH mass, spin, inclination angle, and accretion rate). We thus anticipate substantial utility of this model for interpreting existing and future observations of BH jets.

Acknowledgments

The authors thank Kazunori Akiyama, Yuri Kovalev, and Alexander Plavin for constructive discussion and comments, and the referee for helpful suggestions. We also acknowledge Craig Walker and Jongseo Kim for providing their M87 image reconstructions, and also Alexey Nikonov and Jae-Young Kim for making their own reconstructions available online. Y.T. is grateful for support from JSPS (Japan Society for the Promotion of Science) Overseas Research Fellowship. Support for this work was provided by the NSF through grants AST-1935980 and AST-2034306, and by the Gordon and Betty Moore Foundation through grants GBMF5278 and GBMF10423. This work has been supported in part by the black hole Initiative at Harvard University, which is funded by the John Templeton Foundation (grants 60477, 61479, and 62286) and the Gordon and Betty Moore Foundation (grant GBMF8273).

Appendix A

Electron Number Density Distribution

In this section, we derive the form of the electron number density distribution $f(\gamma)$—where $f(\gamma)d\gamma$ provides the number density of electrons with Lorentz factors in the interval $d\gamma$—given the prescription described in Section 2.3. We assume that the electrons are initially injected with a power-law distribution of Lorentz factors,

$$f_{\rm inj}(\gamma) = \begin{cases} 0, & \gamma < \gamma_m \\ n_m\left(\frac{\gamma}{\gamma_m}\right)^{-p}, & \gamma_m \leqslant \gamma \leqslant \gamma_{\max}, \\ 0, & \gamma > \gamma_{\max} \end{cases} \tag{A1}$$

where γ_m and $\gamma_{\max}$ are the minimum and maximum Lorentz factors of the injected power-law distribution, respectively, n_m is the number density of electrons injected with Lorentz factor γ_m, and p is the power-law index. Here, $n_m = n_{\rm pl}(p-1)/\{\gamma_m^p(\gamma_m^{1-p} - \gamma_{\max}^{1-p})\}$ and $n_{\rm pl}$ is the total number density determined from the Poynting flux as described in Section 2.3. We further assume that the electrons cool via synchrotron radiation. Similar derivations can be found in, e.g., A. G. Pacholczyk (1970), I. Martí-Vidal et al. (2011), and A. Panaitescu (2019).

A.1. Single Injection Event

The total power radiated by an electron with Lorentz factor γ in a magnetic field of strength B is given by

$$\dot{E} = -\frac{\sigma_T c \gamma^2 B^2}{6\pi}. \tag{A2}$$

Given an energy per electron of $E = \gamma m_e c^2$, the corresponding rate of change of the electron's Lorentz factor will be[22]

$$\dot{\gamma} = \frac{\dot{E}}{m_e c^2} = -\frac{\sigma_T \gamma^2 B^2}{6\pi m_e c}. \tag{A3}$$

Assuming that B is constant in time, integrating $\dot{\gamma}$ yields

$$\gamma(t) = \left(\frac{1}{\gamma_0} + \frac{1}{\Gamma(t)}\right)^{-1}, \tag{A4}$$

where γ_0 is the Lorentz factor at $t = 0$ and

$$\Gamma(t) \equiv \frac{6\pi m_e c}{\sigma_T B^2 t}. \tag{A5}$$

Via continuity of electron number, we have for a single injection event

$$f_s(\gamma, t) = f_{\rm inj}(\gamma_0)\frac{d\gamma_0}{d\gamma}, \tag{A6}$$

which evaluates to

---

[21] All the results in this paper are for an observer inclination angle of 163°, based on the analysis of R. C. Walker et al. (2018). To investigate if we could make the counter-jet substantially brighter by using a less extreme viewing angle, we computed an image for an inclination angle of 155°, which is outside the range allowed by R. C. Walker et al. (2018). The counter-jet remains very dim.

[22] Equations (A3) and (A5) are standard results for an isotropic energy distribution function. A more careful analysis, which is left to future work, will need to include the effects of anisotropy.

$$f_s(\gamma, t) = \begin{cases} 0, & \gamma < \left(\frac{1}{\gamma_m} + \frac{1}{\Gamma(t)}\right)^{-1} \\ n_m\left(\frac{\gamma}{\gamma_m}\right)^{-p}\left(1 - \frac{\gamma}{\Gamma(t)}\right)^{p-2}, & \left(\frac{1}{\gamma_m} + \frac{1}{\Gamma(t)}\right)^{-1} \leqslant \gamma \leqslant \left(\frac{1}{\gamma_{\max}} + \frac{1}{\Gamma(t)}\right)^{-1}. \\ 0, & \gamma > \left(\frac{1}{\gamma_{\max}} + \frac{1}{\Gamma(t)}\right)^{-1} \end{cases} \tag{A7}$$

Here, n_m is the number density of electrons injected with Lorentz factor γ_m.

A.2. Continuous Injection

However, the total electron population at some time t_c will actually contain contributions from electron subpopulations that have had cooling times ranging from $t = 0$ up to $t = t_c$, so we need to integrate further. The integral setup looks like

$$f(\gamma) = \frac{\gamma_c}{t_c}\int_0^{t_c} f_s(\gamma, t_c - t)dt\ , \tag{A8}$$

where $\gamma_c \equiv \Gamma(t_c)$ and the γ_c/t_c prefactor ensures that the distribution remains normalized to the injected value. Evaluating this integral requires tracking several possible branches determined by the relative values of various Lorentz factors. Defining

$$\gamma_{\min} \equiv \left(\frac{1}{\gamma_m} + \frac{1}{\gamma_c}\right)^{-1} \tag{A9}$$

and

$$\gamma_{\mathrm{mid}} \equiv \left(\frac{1}{\gamma_{\max}} + \frac{1}{\gamma_c}\right)^{-1}, \tag{A10}$$

the behavior of $n(\gamma)$ depends on the relative values of γ_{mid} and γ_m. If $\gamma_m < \gamma_{\mathrm{mid}}$, then we are in the "slow-cooling regime" and

$$f_{\mathrm{slow}}(\gamma) = \begin{cases} 0, & \gamma < \gamma_{\min} \\ \frac{n_m\gamma_c}{(p-1)\gamma}\left(\frac{\gamma}{\gamma_m}\right)^{-p}\left[\left(\frac{\gamma}{\gamma_m}\right)^{p-1} - \left(1 - \frac{\gamma}{\gamma_c}\right)^{p-1}\right], & \gamma_{\min} \leqslant \gamma < \gamma_m \\ \frac{n_m\gamma_c}{(p-1)\gamma}\left(\frac{\gamma}{\gamma_m}\right)^{-p}\left[1 - \left(1 - \frac{\gamma}{\gamma_c}\right)^{p-1}\right], & \gamma_m \leqslant \gamma < \gamma_{\mathrm{mid}} \quad . \\ \frac{n_m\gamma_c}{(p-1)\gamma}\left(\frac{\gamma}{\gamma_m}\right)^{-p}\left[1 - \left(\frac{\gamma}{\gamma_{\max}}\right)^{p-1}\right], & \gamma_{\mathrm{mid}} \leqslant \gamma < \gamma_{\max} \\ 0, & \gamma \geqslant \gamma_{\max} \end{cases} \tag{A11}$$

Similarly, if $\gamma_m > \gamma_{\mathrm{mid}}$, then we are in the "fast-cooling regime" and

$$f_{\mathrm{fast}}(\gamma) = \begin{cases} 0, & \gamma < \gamma_{\min} \\ \frac{n_m\gamma_c}{(p-1)\gamma}\left(\frac{\gamma}{\gamma_m}\right)^{-p}\left[\left(\frac{\gamma}{\gamma_m}\right)^{p-1} - \left(1 - \frac{\gamma}{\gamma_c}\right)^{p-1}\right], & \gamma_{\min} \leqslant \gamma < \gamma_{\mathrm{mid}} \\ \frac{n_m\gamma_c}{(p-1)\gamma}\left(\frac{\gamma}{\gamma_m}\right)^{-1}\left[1 - \left(\frac{\gamma_m}{\gamma_{\max}}\right)^{p-1}\right], & \gamma_{\mathrm{mid}} \leqslant \gamma < \gamma_m \quad . \\ \frac{n_m\gamma_c}{(p-1)\gamma}\left(\frac{\gamma}{\gamma_m}\right)^{-p}\left[1 - \left(\frac{\gamma}{\gamma_{\max}}\right)^{p-1}\right], & \gamma_m \leqslant \gamma < \gamma_{\max} \\ 0, & \gamma \geqslant \gamma_{\max} \end{cases} \tag{A12}$$

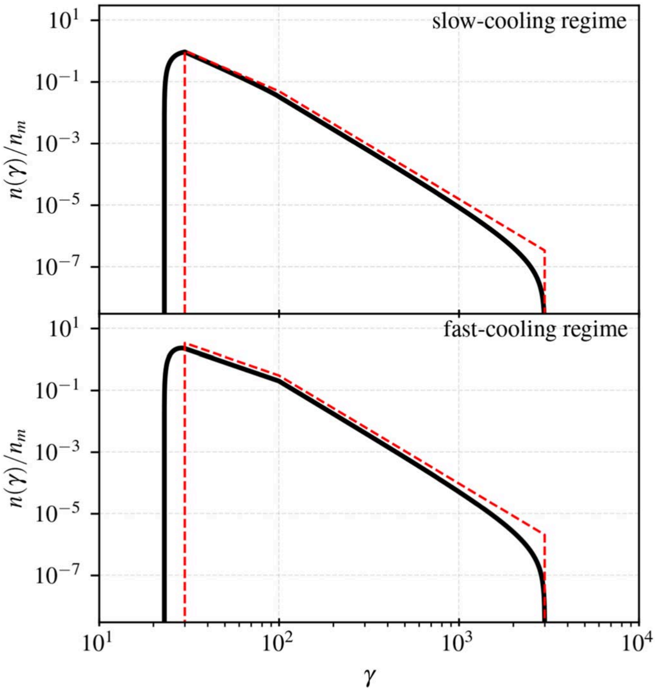

Figure 6. Example electron energy distribution functions corresponding to the slow-cooling (upper panel) and fast-cooling (lower panel) regimes. The solid black curves show the exact distributions from Equations (A11) and (A12), and the red dashed curves show the double power-law approximations from Equations (A13) and (A14). For the upper panel, we have set $\gamma_m = 30$ and $\gamma_c = 100$, while the lower panel uses $\gamma_m = 100$ and $\gamma_c = 30$; we have set $\gamma_{\max} = 3000$ for both panels.

The distributions Equations (A11) and (A12) are shown as the solid black curves in Figure 6.

A.3. Double Power-law Approximation

The distribution functions Equations (A11) and (A12) can be approximated as double power laws (e.g., R. Sari et al. 1998), which simplifies computation of the synchrotron emissivity and absorption coefficients needed for downstream GRRT. The distribution function in the slow-cooling regime ($\gamma_c > \gamma_m$) can be approximated as

$$f_{\text{slow}}(\gamma) \approx \begin{cases} 0, & \gamma < \gamma_m \\ n_m\left(\dfrac{\gamma}{\gamma_m}\right)^{-p}, & \gamma_m \leqslant \gamma < \gamma_c \\ n_m\left(\dfrac{\gamma_c}{\gamma_m}\right)^{-p}\left(\dfrac{\gamma}{\gamma_c}\right)^{-(p+1)}, & \gamma_c \leqslant \gamma < \gamma_{\max} \\ 0, & \gamma \geqslant \gamma_{\max} \end{cases}, \tag{A13}$$

while in the fast-cooling regime ($\gamma_c < \gamma_m$) we have

$$f_{\text{fast}}(\gamma) \approx \begin{cases} 0, & \gamma < \gamma_c \\ n_m\left(\frac{\gamma_m}{\gamma_c}\right)\left(\frac{\gamma}{\gamma_c}\right)^{-2}, & \gamma_c \leqslant \gamma < \gamma_m \\ n_m\left(\frac{\gamma_c}{\gamma_m}\right)\left(\frac{\gamma}{\gamma_m}\right)^{-(p+1)}, & \gamma_m \leqslant \gamma < \gamma_{\max} \\ 0, & \gamma \geqslant \gamma_{\max} \end{cases}. \tag{A14}$$

The distributions of Equations (A13) and (A14) are shown as the dashed red curves in Figure 6.

Appendix B
Anisotropic Double Power-law Synchrotron Emissivity and Absorption Coefficient

To generalize the anisotropic single power-law model in Equation (13) to an anisotropic double power-law distribution function with a lower cutoff at $\gamma = \gamma_{\min}$ and a break at $\gamma = \gamma_{\text{br}}$, we write

$$f(\gamma, \xi) = \begin{cases} N_{\text{wpl}} \quad \gamma^{-p_1}\{1 + (\eta - 1)\cos^2\xi\}^{-p_1/2} & (\gamma_{\min} < \gamma < \gamma_{\text{br}}, \quad 0 \leqslant \xi \leqslant \pi) \\ N_{\text{wpl}} \quad \frac{P(p_1, \eta)}{P(p_2, \eta)}{\gamma_{\text{br}}}^{(p_2 - p_1)} \quad \gamma^{-p_2}\{1 + (\eta - 1)\cos^2\xi\}^{-p_2/2} & (\gamma_{\text{br}} < \gamma < \gamma_{\max}, \quad 0 \leqslant \xi \leqslant \pi) \\ 0 & (\text{ otherwise }). \end{cases} \tag{B1}$$

Here, the two power-law parts are connected at $\gamma = \gamma_{\rm br}$ after integrating over ξ, and $N_{\rm wpl}$ is a normalization factor. Note that, for slow cooling, $\gamma_{\rm min} = \gamma_{\rm m}$, $p_1 = p$, $\gamma_{\rm br} = \gamma_c$, and $p_2 = p + 1$, whereas for fast cooling, $\gamma_{\rm min} = \gamma_{\rm c}$, $p_1 = 2$, $\gamma_{\rm br} = \gamma_m$, and $p_2 = p + 1$.

Normalizing $f(\gamma, \xi)$ by the total number density of power-law electrons $n_{\rm pl}$ yields

$$N_{\rm wpl} = \frac{(p_1 - 1)n_{\rm pl}}{A} P(p_1, \eta)^{-1}, \tag{B2}$$

$$A = \gamma_{\rm min}^{1-p_1} - \gamma_{\rm br}^{1-p_1} + \frac{p_1 - 1}{p_2 - 1}\gamma_{\rm br}^{p_2 - p_1}(\gamma_{\rm br}^{1-p_2} - \gamma_{\rm max}^{1-p_2}). \tag{B3}$$

For $\eta = 1$, Equation (B1) reverts to an isotropic double power-law distribution function (see, for example, T. Kawashima et al. 2023). As the two power-law segments, $\gamma_{\rm min} < \gamma < \gamma_{\rm br}$ and $\gamma_{\rm br} < \gamma < \gamma_{\rm max}$, in Equation (B1) contribute to the two corresponding segments of the γ-integral and are then summed up, the full-polarization, anisotropic double power-law synchrotron emissivities are obtained as

$$j_I = \phi_1(\theta_B) j_{I,{\rm iso1}} + \gamma_{\rm br}^{p_2 - p_1}\phi_2(\theta_B) j_{I,{\rm iso2}}, \tag{B4}$$

$$j_Q = \phi_1(\theta_B) j_{Q,{\rm iso1}} + \gamma_{\rm br}^{p_2 - p_1}\phi_2(\theta_B) j_{Q,{\rm iso2}}, \tag{B5}$$

$$j_U = 0, \tag{B6}$$

$$j_V = \phi_1(\theta_B)\left\{1 + \frac{g_1(\theta_B)}{p_1 + 2}\right\} j_{V,{\rm iso1}} + \gamma_{\rm br}^{p_2 - p_1}\phi_2(\theta_B)\left\{1 + \frac{g_2(\theta_B)}{p_2 + 2}\right\} j_{V,{\rm iso2}}, \tag{B7}$$

where

$$\phi_1(\theta_B) = P(p_1, \eta)^{-1}\{1 + (\eta - 1)\cos^2\theta_B\}^{-p_1/2},$$
$$\phi_2(\theta_B) = P(p_2, \eta)^{-1}\{1 + (\eta - 1)\cos^2\theta_B\}^{-p_2/2}, \tag{B8}$$

$$g_1(\theta_B) = \frac{p_1(\eta - 1)\sin^2\theta_B}{1 + (\eta - 1)\cos^2\theta_B}, \quad g_2(\theta_B) = \frac{p_2(\eta - 1)\sin^2\theta_B}{1 + (\eta - 1)\cos^2\theta_B}. \tag{B9}$$

Here, $j_{\{I,Q,V\},{\rm iso1}}$ and $j_{\{I,Q,V\},{\rm iso2}}$ are the isotropic single power-law emissivities for $\gamma_{\rm min} < \gamma < \gamma_{\rm br}$ with power-law index p_1 and $\gamma_{\rm br} < \gamma < \gamma_{\rm max}$ with p_2, respectively, with the total number density of power-law electron given by $n_{\rm pl}$. The absorption coefficients are also obtained in an analogous way as follows:

$$\alpha_I = \phi_1(\theta_B)\alpha_{I,{\rm iso1}} + \gamma_{\rm br}^{p_2 - p_1}\phi_2(\theta_B)\alpha_{I,{\rm iso2}}, \tag{B10}$$

$$\alpha_Q = \phi_1(\theta_B)\alpha_{Q,{\rm iso1}} + \gamma_{\rm br}^{p_2 - p_1}\phi_2(\theta_B)\alpha_{Q,{\rm iso2}}, \tag{B11}$$

$$\alpha_U = 0, \tag{B12}$$

$$\alpha_V = \phi_1(\theta_B)\left\{1 + \frac{g_1(\theta_B)}{p_1 + 2}\right\}\alpha_{V,{\rm iso1}} + \gamma_{\rm br}^{p_2 - p_1}\phi_2(\theta_B)\left\{1 + \frac{g_2(\theta_B)}{p_2 + 2}\right\}\alpha_{V,{\rm iso2}}. \tag{B13}$$

Appendix C
Poynting Flux

In our model, we set the nonthermal electron energy density by requiring that it be proportional to the magnitude of the Poynting vector $\boldsymbol{S}$ (see Equation (7)). However, $|\boldsymbol{S}|$ is a frame-dependent quantity, so we must choose a frame in which to perform this density normalization. In the Kerr spacetime, the natural candidate is the Zero-Angular-Momentum (ZAMO) frame, which remains timelike everywhere in the black hole exterior and is given in Boyer–Lindquist coordinates by

$$n_\mu = (-\alpha, 0, 0, 0) \tag{C1}$$

with $\alpha = (-g^{tt})^{-1/2}$.

The Poynting flux four-vector in the ZAMO frame is given by an appropriate projection of the stress energy, $T^{\mu\nu}_{\rm EM}$:

$$S^\mu = (n^\mu n_\nu + \delta^\mu_\nu)(-n_\alpha T^{\alpha\nu}_{\rm EM}). \tag{C2}$$

This definition of S^μ is equivalent to the electromagnetic part of the energy flux vector perpendicular to the normal observer, $\tilde{Q}^\mu$ in S. C. Noble et al. (2006). The magnitude of the normal observer Poynting flux is

$$|\vec{S}|_{\rm ZAMO} = \sqrt{S^\mu S_\mu} = \sqrt{v_\perp^2 \mathcal{B}^4}, \tag{C3}$$

where $v_\perp$ is the field-perpendicular fluid velocity as measured in the ZAMO frame, and $\mathcal{B}$ is the magnetic field strength as measured in the ZAMO frame. Both quantities can be defined covariantly as

$$v_\perp^\mu = \frac{u^\mu}{\gamma} - v_\parallel \frac{\mathcal{B}^\mu}{\sqrt{\mathcal{B}^2}} - n^\mu, \qquad \mathcal{B}^\mu = n_\nu(\star F)^{\nu\mu}, \tag{C4}$$

with u^μ being the plasma four-velocity, $\star F$ the Faraday dual, $\gamma = -u_\mu n^\mu$ the ZAMO frame Lorentz factor, and $v_\parallel = u_\mu \mathcal{B}^\mu / \gamma\sqrt{\mathcal{B}^2}$ the ZAMO frame field-parallel velocity. Furthermore, one can show (e.g., A. Chael 2024, Equation (24) in that paper) that $v_\perp^2 = \mathcal{E}^2/\mathcal{B}^2$, where $\mathcal{E}^\mu = n_\nu F^{\mu\nu}$ is the ZAMO frame electric field, such that

$$|\boldsymbol{S}|_{\rm ZAMO} = \sqrt{\mathcal{E}^2\mathcal{B}^2}. \tag{C5}$$

One can alternatively derive Equations (C3) and (C5) by explicitly constructing an orthonormal tetrad for the ZAMO frame. Since this orthonormal frame is locally Minkowski, one can use $\boldsymbol{S} = \frac{c}{4\pi}\boldsymbol{E} \times \boldsymbol{B}$, with $\boldsymbol{E}$ and $\boldsymbol{B}$ being the electromagnetic three-vectors computed from the tetrad. Then, upon successive application of vector identities combined with the definition of the drift velocity, one can simplify the cross product to arrive at Equation (C3).

Appendix D
Role of the Sigma Cutoff

In the third and fourth panels in Figure 1, we have applied the sigma cutoff prescription given in Equation (2) in order to limit the region of the GRMHD model that is included when computing the image. Applying a sigma cutoff is very common because the high-sigma regions of a GRMHD simulation are prone to large numerical errors. The very low density in these regions causes numerical difficulties that require the application of density floors and other numerical fixes to stabilize the simulation. This is, of course, at the cost of accuracy. In much

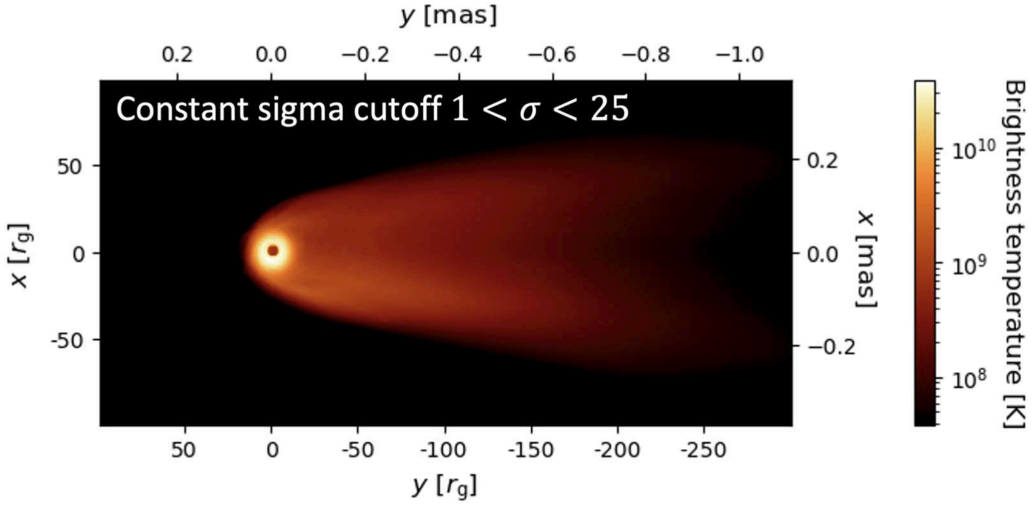

Figure 7. Same as the bottom panel of Figure 1, but with a constant sigma cutoff for nonthermal emission: $1 < \sigma < 25$ (based on A. Chael 2024).

of the work of the EHT Collaboration, a severe cutoff of $\sigma_m = 1$ is applied (e.g., Event Horizon Telescope Collaboration et al. 2019d). Although this cuts out a large part of the jet volume, this is of little consequence for studies that focus on the BH shadow.

For studies of the jet, however, it is necessary to relax the sigma cutoff criterion, and there has been some previous discussion (e.g., A. Chael et al. 2019). In an important recent study, A. Chael (2024) carried out hybrid GRMHD+GRFFE simulations that treat the jet funnel region more accurately using force-free equations. By comparing the results with those from traditional GRMHD simulations, he finds that GRMHD simulation results may be trusted for σ values up to $\sigma_m = 25$, but regions with larger σ are problematic.[23] Our cutoff prescription (Equation (2)) is more stringent than Chael's limit for projected distances $y > 40r_g$ in the jet. A natural question then is: How much of the limb-brightening we obtained in the bottom panel in Figure 1 is from our severe sigma cutoff Equation (2) rather from our introduction of anisotropy in the electrons?

To answer this question, we show in Figure 7 the time-averaged image we obtain when we use the A. Chael (2024) constant sigma cutoff of $\sigma_m = 25$ for calculating the nonthermal radiation from the jet. We confirm that, even with this less severe sigma cutoff, the image still gives a limb-brightened jet, which looks essentially the same as in the fiducial model image in the bottom panel in Figure 1. Therefore, the limb-brightening is primarily from introducing anisotropy in the electron distribution. A more detailed comparison reveals that the image in Figure 7 is dimmer near the inner ring and brighter in the outer jet compared to the fiducial model, since the $\sigma_m = 25$ cutoff excludes a larger volume of the jet near the BH but a narrower region in the outer funnel, relative to Equation (2).

ORCID iDs

Yuh Tsunetoe https://orcid.org/0000-0003-0213-7628
Dominic W. Pesce https://orcid.org/0000-0002-5278-9221
Ramesh Narayan https://orcid.org/0000-0002-1919-2730
Andrew Chael https://orcid.org/0000-0003-2966-6220
Zachary Gelles https://orcid.org/0000-0001-8053-4392
Charles Gammie https://orcid.org/0000-0001-7451-8935
Eliot Quataert https://orcid.org/0000-0001-9185-5044
Daniel Palumbo https://orcid.org/0000-0002-7179-3816

References

Abramowski, A., Acero, F., Aharonian, F., et al. 2012, ApJ, 746, 151
Arras, P., Knollmüller, J., Junklewitz, H., & Enßlin, T. A. 2018, arXiv:1803.02174
Bale, S. D., Kasper, J. C., Howes, G. G., et al. 2009, PhRvL, 103, 211101,
Blandford, R. D., & Königl, A. 1979, ApJ, 232, 34
Blandford, R. D., & Znajek, R. L. 1977, MNRAS, 179, 433
Bridle, A. H., & Perley, R. A. 1984, ARA&A, 22, 319
Broderick, A. E., & Loeb, A. 2009, ApJ, 697, 1164
Bronzwaer, T., Davelaar, J., Younsi, Z., et al. 2018, A&A, 613, A2
Camporeale, E., & Burgess, D. 2008, JGRA, 113, A07107
Chael, A. 2024, MNRAS, 532, 3198
Chael, A., Lupsasca, A., Wong, G. N., & Quataert, E. 2023, ApJ, 958, 65
Chael, A., Narayan, R., & Johnson, M. D. 2019, MNRAS, 486, 2873
Chael, A. A., Narayan, R., & Sadowski, A. 2017, MNRAS, 470, 2367
Chandra, M., Gammie, C. F., Foucart, F., & Quataert, E. 2015, ApJ, 810, 162
Comisso, L., & Jiang, B. 2023, ApJ, 959, 137
Comisso, L., & Sironi, L. 2021, PhRvL, 127, 255102
Comisso, L., & Sironi, L. 2022, ApJL, 936, L27
Cranmer, S. R., Kohl, J. L., Noci, G., et al. 1999, ApJ, 511, 481
Cruz-Osorio, A., Fromm, C. M., Mizuno, Y., et al. 2022, NatAs, 6, 103
Davelaar, J., Olivares, H., Porth, O., et al. 2019, A&A, 632, A2
Dexter, J. 2016, MNRAS, 462, 115
Dexter, J., Agol, E., Fragile, P. C., & McKinney, J. C. 2010, ApJ, 717, 1092
Doeleman, S. S., Barrett, J., Blackburn, L., et al. 2023, Galax, 11, 107
Event Horizon Telescope Collaboration, Akiyama, K., Alberdi, A., et al. 2019a, ApJL, 875, L5
Event Horizon Telescope Collaboration, Akiyama, K., Alberdi, A., et al. 2019b, ApJL, 875, L1
Event Horizon Telescope Collaboration, Akiyama, K., Alberdi, A., et al. 2019c, ApJL, 875, L2
Event Horizon Telescope Collaboration, Akiyama, K., Alberdi, A., et al. 2019d, ApJL, 875, L3
Event Horizon Telescope Collaboration, Akiyama, K., Alberdi, A., et al. 2019e, ApJL, 875, L4
Event Horizon Telescope Collaboration, Akiyama, K., Alberdi, A., et al. 2019f, ApJL, 875, L6
Event Horizon Telescope Collaboration, Akiyama, K., Algaba, J. C., et al. 2021a, ApJL, 910, L13
Event Horizon Telescope Collaboration, Akiyama, K., Algaba, J. C., et al. 2021b, ApJL, 910, L12

---

[23] An additional consideration is that most GRMHD simulations apply so-called reflecting boundary conditions at the poles, which means that the first couple of cells around $\theta = 0$ and π must be ignored. A sigma cutoff naturally eliminates this region.

Event Horizon Telescope Collaboration, Akiyama, K., Alberdi, A., et al. 2023, ApJL, 957, L20

Ferraro, V. C. A. 1937, MNRAS, 97, 458

Fromm, C. M., Cruz-Osorio, A., Mizuno, Y., et al. 2022, A&A, 660, A107

Galishnikova, A., Philippov, A., & Quataert, E. 2023, ApJ, 957, 103

Gammie, C. F., McKinney, J. C., & Tóth, G. 2003, ApJ, 589, 444

Gelles, Z., Chael, A., & Quataert, E. 2025, ApJ, 981, 204

Giovannini, G., Savolainen, T., Orienti, M., et al. 2018, NatAs, 2, 472

Hada, K. 2017, Galax, 5, 2

Hada, K., Kino, M., Doi, A., et al. 2013, ApJ, 775, 70

Hada, K., Kino, M., Doi, A., et al. 2016, ApJ, 817, 131

Harris, D. E., & Krawczynski, H. 2006, ARA&A, 44, 463

Igumenshchev, I. V., Narayan, R., & Abramowicz, M. A. 2003, ApJ, 592, 1042

Janssen, M., Falcke, H., Kadler, M., et al. 2021, NatAs, 5, 1017

Johnson, M. D., Akiyama, K., Baturin, R., et al. 2024, Proc. SPIE, 13092, 130922D

Kawashima, T., Ohsuga, K., & Takahashi, H. R. 2023, ApJ, 949, 101

Kim, J.-S., Mueller, H., Nikonov, A. S., et al. 2024a, arXiv:2409.00540

Kim, J.-S., Nikonov, A. S., Roth, J., et al. 2024b, A&A, 690, A129

Kim, J. Y., Krichbaum, T. P., Lu, R. S., et al. 2018, A&A, 616, A188

Lu, R.-S., Asada, K., Krichbaum, T. P., et al. 2023, Natur, 616, 686

Marshall, H. L., Miller, B. P., Davis, D. S., et al. 2002, ApJ, 564, 683

Martí-Vidal, I., Pérez-Torres, M. A., & Brunthaler, A. 2011, A&A, 529, A47

McKinney, J. C. 2006, MNRAS, 368, 1561

Melrose, D. B. 1971, Ap&SS, 12, 172

Mościbrodzka, M., Falcke, H., & Shiokawa, H. 2016, A&A, 586, A38

Nakamura, M., Asada, K., Hada, K., et al. 2018, ApJ, 868, 146

Narayan, R., Chael, A., Chatterjee, K., Ricarte, A., & Curd, B. 2022, MNRAS, 511, 3795

Narayan, R., Igumenshchev, I. V., & Abramowicz, M. A. 2003, PASJ, 55, L69

Narayan, R., McKinney, J. C., & Farmer, A. J. 2007, MNRAS, 375, 548

Nikonov, A. S., Kovalev, Y. Y., Kravchenko, E. V., Pashchenko, I. N., & Lobanov, A. P. 2023, MNRAS, 526, 5949

Noble, S. C., Gammie, C. F., McKinney, J. C., & Del Zanna, L. 2006, ApJ, 641, 626

Okamoto, I. 1974, MNRAS, 167, 457

Pacholczyk, A. G. 1970, Radio Astrophysics. Nonthermal Processes in Galactic and Extragalactic Sources (W. H. Freeman and Company)

Panaitescu, A. 2019, ApJ, 886, 106

Park, J., Hada, K., Kino, M., et al. 2019, ApJ, 887, 147

Park, J., Zhao, G.-Y., Nakamura, M., et al. 2024, ApJL, 973, L45

Perlman, E. S., Adams, S. C., Cara, M., et al. 2011, ApJ, 743, 119

Sari, R., Piran, T., & Narayan, R. 1998, ApJL, 497, L17

Sadowski, A., Narayan, R., McKinney, J. C., & Tchekhovskoy, A. 2014, MNRAS, 439, 503

Sadowski, A., Narayan, R., Tchekhovskoy, A., & Zhu, Y. 2013, MNRAS, 429, 3533

Sironi, L., Rowan, M. E., & Narayan, R. 2021, ApJL, 907, L44

Sturrock, P. A. 1994, Plasma Physics, An Introduction to the Theory of Astrophysical, Geophysical and Laboratory Plasmas (Cambridge: Cambridge Univ. Press)

Takahashi, K., Toma, K., Kino, M., Nakamura, M., & Hada, K. 2018, ApJ, 868, 82

Tchekhovskoy, A., McKinney, J. C., & Narayan, R. 2008, MNRAS, 388, 551

Tchekhovskoy, A., Narayan, R., & McKinney, J. C. 2011, MNRAS, 418, L79

Tsunetoe, Y., Kawashima, T., Ohsuga, K., & Mineshige, S. 2024, PASJ, 76, 1211

Tsunetoe, Y., Narayan, R., & Ricarte, A. 2025, ApJ, 983, 77

Walker, R. C., Hardee, P. E., Davies, F. B., Ly, C., & Junor, W. 2018, ApJ, 855, 128

Yang, H., Yuan, F., Li, H., et al. 2024, SciA, 10, eadn3544

Yuan, F., & Narayan, R. 2014, ARA&A, 52, 529

Zhang, M., Mizuno, Y., Fromm, C. M., Younsi, Z., & Cruz-Osorio, A. 2024, A&A, 687, A88

Zhdankin, V., Kunz, M. W., & Uzdensky, D. A. 2023, ApJ, 944, 24